Polarimetric Size Sorting Signatures in the Convective Regions of Mesoscale Convective Systems in PECAN: Implications on Kinematics, Thermodynamics, and Precipitation Pathways

Frederick Iat-Hin Tam[1], Ming-Jen Yang[1#], Wen-Chau Lee[2]

[1]National Taiwan University, Taipei, Taiwan

[2]National Center for Atmospheric Research

Submitted to *Journal of Geophysical Research – Atmospheres*

September 2021

#Corresponding author:

Dr. Ming-Jen Yang, Dept. of Atmospheric Sciences, National Taiwan University

No.1 Sec. 4 Roosevelt Road, Taipei, 10617, Taiwan

Email: `mingjen@as.ntu.edu.tw`

Key Points:

- A positive correlation exists between the magnitudes of size sorting signatures and convective depth.
- Larger size sorting magnitudes are associated with more riming growth and quicker graupel fallout.
- Intense convective precipitation in the PECAN MCSs seems to be dominated more by cold rain processes than warm rain processes.

ABSTRACT

An object-based technique was utilized to identify hydrometeor size-sorting signatures at lower levels in the convective regions of 10 mesoscale convective systems (MCSs) during the 2015 Plains Elevated Convection at Night (PECAN) field campaign. Composite statistical analysis indicates that the magnitudes of size-sorting signatures (the separation distances between rain diameter maxima and concentration maxima) are nonlinearly correlated to the echo-top height, rain mass beneath the melting level, and precipitation rates at higher percentiles. To explore this correlation, the WRF model was used to simulate one of the MCSs (the 20 June 2015 storm) during the PECAN. Statistical analysis on the model outputs indicates more active riming growth and quicker graupel fallout at warmer temperatures near areas with larger separation distances. While updraft intensity above the melting level was also positively correlated to separation distances, this correlation was only statistically significant within certain temperature ranges. Additional analyses reveal that the higher intense precipitation potential near signatures with large separation distances could be attributed to precipitation production from the melted graupel. Finally, spatial correspondence between graupel distribution at the melting level and rain

distribution at the lowest model level illustrates the critical role of graupel sedimentation and sorting in creating size-sorting signatures in MCSs during the PECAN field experiment.

Plain Language Summary:

In this manuscript, we have examined the hydrometeor size-sorting signatures from the polarimetric radar parameters observed in the convective regions from 10 mesoscale convective systems during the 2015 PECAN field campaign. A model simulation for one of the storms is conducted to verify the composite statistical analyses from radar observations. We believe that these findings would be interesting to radar and microphysics scientists and general readers.

1. Introduction

Understanding the microphysical processes of organized mesoscale convective systems (MCSs) and accurately parameterizing the microphysical processes on MCSs in numerical models remain a great challenge for weather forecasters and scientists. One of the factors limiting the improvement in the prediction of storm microphysics is the lack of three-dimensional observations on the drop size distributions (DSDs) of hydrometeors within the MCSs. Biases in the DSDs have substantial impacts on model performance. Idealized numerical simulations have shown that prescribed raindrop DSDs and the treatment of raindrop breakup and size sorting yield substantial influences on the MCS characteristics like cold-pool intensity and low-level lifting through raindrop evaporation (Dawson et al., 2010; Morrison et al., 2012; Planche et al. 2019). In practice, we mostly rely on research flights and disdrometers to acquire *in-situ* measurements of hydrometeor DSDs. However, airborne measurements are costly and only limited observation data can be collected during field campaigns. An advantage of airborne in-situ measurements is that they capture DSD variabilities in the vertical within the storm (Stechman et al., 2020a) during flight hours. Ground-based disdrometers cannot capture DSD vertical variabilities, but can provide *surface* DSD measurements over longer period of time.

Polarimetric radars provide an alternative method to estimate the three-dimensional DSD information in weather systems with greater spatial details and higher temporal frequency. Among various polarimetric variables, differential reflectivity (Z_{DR}) and specific differential propagation phase (K_{DP}) are particularly useful in characterizing the DSDs. The Z_{DR} is the ratio between reflectivity factors in the horizontal and vertical polarizations. The Z_{DR} reveals the dominant particle shape within a radar sampling volume, with Z_{DR}>0 dB indicating the volume to be dominated by oblate particles. The K_{DP} measures the range-dependent phase changes of the horizontally- and vertically-polarized radar waves. Positive K_{DP} are expected in areas with (a) high concentration of oblate rain drops, (b) small melting hailstones, and (c) aggregates of oblate ice crystals (Rauber and Nesbitt, 2018).

The use of polarimetric radars for severe weather systems has revealed the DSD signatures which were unobserved previously. These signatures include the en-

hanced Z_{DR} along reflectivity gradients in the forward flanks of supercells (Z_{DR} arcs; Kumjian and Ryzhkov, 2008; Dawson et al., 2014), and the Z_{DR}-K_{DP} separations in different shear quadrants of hurricane eyewalls (Didlake and Kumjian, 2018; Feng and Bell, 2018; Laurencin et al., 2020). Hydrometeor size sorting, which is produced by differential advection and sedimentation of hydrometeors of different sizes due to updraft and fall-speed differences, is the essential process producing these DSD signatures.

While observational studies of hydrometeor size sorting are plentiful in the literature, further investigation is still needed to clarify the uncertainties in this process. The first uncertainty is how the size sorting of ice hydrometeors contributes to the variabilities of low-level rain DSD. Dawson et al. (2015; hereafter DMR15) showed that inputting supercell hodographs to a rain sedimentation model was sufficient in producing the low-level DSD variabilities which were similar to the Z_{DR} arcs. Similarly, Laurencin et al. (2020; hereafter LDL20) reported that applying the low-level winds of Hurricane Matthew (2016) to an analytical model recreated the Z_{DR}-K_{DP} azimuthal separation in Matthew's eyewall. However, DMR15 and LDL20 restricted their investigation to the sorting of rain shafts with prescribed DSDs and did not consider ice sorting aloft. Indeed, numerical simulations with free-evolving DSDs of ice particles indicated that deep-layer storm-relative winds and the sorting of hail particles are more important than the sorting of raindrops in producing the Z_{DR} arcs in the left flank of right-moving supercells (Dawson et al., 2014). The second uncertainty is the role of updrafts. While both updrafts and storm-relative winds can lead to sustained size sorting (Kumjian and Ryzhkov, 2012), previous studies (e.g., DMR15; Feng and Bell, 2018; LDL20; Loeffler et al., 2020) mostly focused on storm-relative winds. These studies implicitly assumed that the effect of storm-relative winds overwhelmed that of the updrafts. This assumption is reasonable for supercells and tropical cyclones (TCs), which have intense horizontal cyclonic flows. Whether this assumption is suitable for other weather systems still remains an open question. For example, updrafts may be more important in regulating the size-sorting signatures in squall-line MCSs, where the circulations are more two-dimensional than those in supercells.

In addition to addressing the above uncertainties, we are also interested to know whether or not size-sorting signatures can be used to evaluate convective variabilities. Yuter and Houze (1995b) suggested that hydrometeor trajectories in MCSs could be understood by the "particle fountain" model. Larger hydrometeors formed in updraft cores sediment closer to the updrafts due to gravity sorting, whereas smaller hydrometeors sediment further rearward as updraft cores expanded and advected rearward by the front-to-rear flow. According to this "particle fountain" model, we hypothesize that larger size-sorting magnitude would positively correlate to ice growth, rearward advection of smaller ice hydrometeors, and updraft intensity. If a positive correlation between size-sorting magnitude and updraft strength could be found, we suggest that the size-sorting magnitude could potentially be used to infer other convective characteristics, such as latent heating and precipitation. Our inference is based on

(a) greater positive buoyancy and latent heat release in stronger updrafts, and (b) higher amount of large ice hydrometeors in stronger updrafts, which could elevate the amount of rain associated with melting ice particles (cold pathway; Lasher-Trapp et al., 2018).

In this study, an object-based technique was applied to 74.5 hours of radar observation data to identify the size-sorting signatures in ten nocturnal MCSs occurred during the 2015 Plains Elevated Convective at Night (PECAN; Geerts et al., 2017) field campaign. The magnitudes of these size-sorting signatures are compared to examine various convective characteristics, emphasizing on identifying trends between the size-sorting magnitude, convective intensity, and precipitation intensity. To compliment the observational analysis, a numerical simulation of the MCS on 20 June 2015 during the PECAN campaign is also conducted to investigate the dependence of statistical trends to different microphysical processes. In summary, this study will address the following three scientific questions:

1. Are the magnitudes of hydrometeor size-sorting signatures in nocturnal MCSs statistically related to convective updraft characteristics?
2. If the hydrometeor size-sorting magnitudes are related to updraft strengths, what microphysical processes contribute the most to this relationship?
3. To what extent can we use hydrometeor size-sorting magnitudes to diagnose the relative contributions of microphysical processes to convective thermodynamics and precipitation pathway?

2. Data sources and analysis technique

2.1 Polarimetric radar observations

We utilized the level-II polarimetric products from the Next Generation Weather Radar (NEXRAD) WSR-88D network to examine hydrometeor size-sorting signatures in the convective regions from 10 nocturnal MCSs during the PECAN field campaign (Table 1). NEXRAD radars performed regular plain position indicator (PPI) scans at 14 elevation angles, with a typical volume scan of 5–12 minutes. The Python ARM Radar Toolkit (Py-ART; Helmus and Collis, 2016) was used to merge radar observations onto a Cartesian grid with the horizontal grid spacing of 1 km and the vertical grid spacing of 0.5 km. The main radar parameters analyzed in this study are radar reflectivity (Z), differential reflectivity (Z_{DR}), and specific differential propagation phase (K_{DP}). Systematic biases in Z_{DR} observations were calibrated using the observations in dry aggregates, which are known to have very small Z_{DR} values (Ryzhkov and Zrnic, 1998). The K_{DP} parameters were derived with the procedure outlined in Lang et al. (2007). The differential phase (ϕ_{DP}) was filtered with a 21-gate finite-impulse response filter, and the half slope of a line fitted to the filtered ϕ_{DP} was defined as the K_{DP}. Non-meteorological signal returns were removed with an insect-filtering algorithm (Lang et al., 2007) and a reflectivity texture-

based ground-clutter removal technique (Gabella and Notarpietro, 2002). Radar gates with correlation coefficients (ρ_{hv}) less than 0.8 were not included in the compositing procedure. Besides the systematic bias, Z_{DR} measurements can be also biased by non-uniform beam filling (NUBF) and depolarization streaks. These artifacts are mostly common at distant ranges and downstream of convective cells. Following Homeyer and Kumjian (2014), we mitigated these biases by merging radar observations taken at different locations and viewing angles into a range-weighted composite. To further reduce the contamination from the NUBF and depolarization streaks, observations that were not within 200 km from individual radars were discarded from the analysis.

2.2 WRF simulations on selected PECAN MCS cases

The MCS on 20 June 2015 was simulated using Version 3.9 of the Weather Forecasting and Research (WRF; Skamarock et al., 2008) Model. The simulation was performed with a triple-nested model domain with 27-, 9-, and 3-km grid spacing, respectively. Three WRF domains are shown in Fig. 1. All domains contained 55 vertical levels, with greater vertical resolution near the melting level (~4 km) and boundary layer. The WRF model was initialized with the 32-km NCEP North American Regional Reanalysis (NARR; Mesinger et al., 2006) data at 1500 UTC 19 June and ran for 48 hours. The NARR wind (u, v) and temperature (T) fields above the boundary layer were nudged every three hours for the first 30 hours of the simulation period to improve the representation of synoptic conditions. The model setting and physical parameterizations for the WRF simulation are listed in Table 2.

2.3 Object-based identification of low-level size sorting signatures

The algorithm used to identify low-level size-sorting signatures in convective regions within MCSs is similar to that originally proposed for non-supercellular tornadic storms (Loeffler and Kumjian, 2018) and supercellular storms (Loeffler et al., 2020). The first part of the algorithm involves identifying the geometrical centers (i.e., the centroids) of different Z_{DR} and K_{DP} objects at 1-km height AGL. The Z_{DR} and K_{DP} objects were defined as the contiguous areas with enhanced Z_{DR} and K_{DP}. Manually-adapted magnitude thresholds were used to produce different objects. A 90-percentile magnitude threshold was used to produce "first guess" objects. These initial objects were adjusted manually to ensure that they accurately outlined the Z_{DR} and K_{DP} enhancements at convective scale. The percentile thresholds used ranged from 90 to 95. We further applied a 75-percentile threshold to remove small artifacts. Finally, the centroid coordinates for each object were found and stored separately. While this method has some inherent subjectivity, large variability in Z_{DR} and K_{DP} values in convective regions makes it difficult to determine a threshold suitable for all cases and all times (Martinaitis, 2017). An automatic method with fixed thresholds may fail to identify Z_{DR} and K_{DP} objects at suitable spatial scales.

The second part of the identification algorithm involves matching different Z_{DR} and K_{DP} objects. A Z_{DR} object was matched to a K_{DP} object if it satisfies

the following criteria: (a) the separation distance between the centroids was smallest for all object combinations, where the separation distance ($d_{\rm obs}$) was the geometrical distance between the centroid of a Z_{DR} object ($x_{Z_{\rm DR}}$, $y_{Z_{\rm DR}}$) and the centroid of a K_{DP} object ($x_{K_{\rm DP}}$, $y_{K_{\rm DP}}$) as

$$d_{\rm obs} = \sqrt{\left(x_{Z_{\rm DR}} - x_{K_{\rm DP}}\right)^2 + \left(y_{Z_{\rm DR}} - y_{K_{\rm DP}}\right)^2}; \quad (1)$$

(b) for a Z_{DR} object, there was at least one K_{DP} object where the $d_{\rm obs}$ was less than 25 km; and (c) the angle between centroids ($\theta_{\rm obs}$) was close to the direction of MCS movement, where the angle was defined as

$$\theta_{\rm obs} = \tan^{-1}\left(\frac{y_{Z_{\rm DR}} - y_{K_{\rm DP}}}{x_{Z_{\rm DR}} - x_{K_{\rm DP}}}\right). \quad (2)$$

Separation distances ($d_{\rm obs}$) was used herein as a quantitative measurement of size-sorting magnitudes. Matched Z_{DR} and K_{DP} objects are denoted as "size-sorting objects" hereafter.

Since radar polarimetric products cannot be directly predicted by the WRF model, the mass-mean rain diameter D_{mr} and the total rain number concentration N_{Tr} were used as proxies for Z_{DR} and K_{DP}, respectively. The mass-mean rain diameter D_{mr} was determined from WRF model outputs with the relationship by Dawson et al. (2014) as

$$D_{\rm mr} = \left(\frac{6\rho_{\rm air} q_r}{\pi \rho_r N_r}\right)^{\frac{1}{3}}, \quad (3)$$

where $\rho_{\rm air}$ is the air density, q_r is the rain mixing ratio, and ρ_r is the bulk rain density. The WRF-equivalent separation distance ($d_{\rm WRF}$), similar to the observation separation distance ($d_{\rm obs}$), was defined as the geometrical distance between the centroid of the mass-mean rain diameter D_{mr} object ($x_{D_{\rm mr}}$, $y_{D_{\rm mr}}$) and the centroid of the total rain number concentration N_{Tr} object ($x_{N_{\rm Tr}}$, $y_{N_{\rm Tr}}$) as

$$d_{\rm WRF} = \sqrt{\left(x_{D_{\rm mr}} - x_{N_{\rm Tr}}\right)^2 + \left(y_{D_{\rm mr}} - y_{N_{\rm Tr}}\right)^2}, \quad (4)$$

and the WRF-equivalent angle between centroids ($\theta_{\rm WRF}$) was defined as

$$\theta_{\rm WRF} = \tan^{-1}\left(\frac{y_{D_{\rm mr}} - y_{N_{\rm Tr}}}{x_{D_{\rm mr}} - x_{N_{\rm Tr}}}\right). \quad (5)$$

Figure 2 shows an example of size-sorting objects simultaneously identified at a particular time (0515 UTC on 5 June 2015) with the identification algorithm given above. The algorithm identified two areas with locally enhanced Z_{DR} and K_{DP} magnitudes near the system edge. The area near $X = 75$ km was of a large d_{obs}, whereas the area near $X = 105$ km was of a smaller d_{obs}. While there were several areas with enhanced K_{DP} in the rear of the system, these areas were filtered out because they were either too small or the Z_{DR} values near these K_{DP} areas did not exceed the magnitude threshold.

2.4 Determining local characteristics near size-sorting objects

In the following sections, kinematics, microphysical and thermodynamic fields near the size-sorting objects were extracted and compared to their separation distances. Values collocated to a particular size-sorting object were the 75 percentile of different variables within a 12-km diameter circle, and the center of the circle was at the midpoint between Z_{DR} (D_{mr}) and K_{DP} (N_{Tr}) centroids.

Since the collocation was performed at each time step, the output value represents the *instantaneous* measurement of each variable near each size-sorting object. This approach may be problematic for several reasons. Firstly, the algorithm outputs may be biased against slower microphysical processes (e.g., snow melting). Secondly, the algorithm outputs may misrepresent the true "local characteristics" near sloped updrafts if the collocation was done in a point-to-point manner. The approach adopted in this study, which derived collocated variables from the environment surrounding each size-sorting object, may help to minimize these uncertainties.

It is known that the thermodynamic structures of convective regions within MCSs are distinct from those of the stratiform regions (Gallus and Johnson, 1991; Braun and Houze, 1996). Hence, the relationship between local MCS kinematics and $d_{\rm obs}/d_{\rm WRF}$ could be dependent upon their locations in the MCS. To remove this ambiguity, the radar reflectivity (Z)-based method of Steiner et al. (1995) was used to partition the radar data at 2-km height into convective and stratiform regions. All objects that were not within the convective regions were discarded from analysis.

The size-sorting object dataset used herein consists of 3996 objects that were identified from NEXRAD observations on ten MCSs during the PECAN field campaign (Table 1). For the 20 June MCS simulated by the WRF, totally 250 objects, identified between 0600 and 1030 UTC, were used to produce the statistical results shown in Section 5.

3. Statistical characteristics of the observed PECAN MCS size-sorting objects

Figure 3a shows the bivariate distribution of PECAN MCS composite between separation distance ($d_{\rm obs}$) and the 20-dBZ echo-top height (ETH). Scatter points represent the ETHs collocated to each object, whereas contours represent the normalized frequency distribution. The contours in Figure 3a show that objects with smaller $d_{\rm obs}$ were mostly associated with lower ETHs. The ETH versus separation distance ($d_{\rm obs}$) distribution for each PECAN MCS indicates a large case-dependent variability, however. While 8 out of 11 PECAN MCSs exhibited increases in ETHs with the increasing $d_{\rm obs}$ (not shown), the $d_{\rm obs}$ magnitude changed where this increase began and the increase rate varied between cases.

In addition to kinematics, we are also curious whether or not the separation distance $d_{\rm obs}$ can be used to infer other convective variabilities. Figure 3b show the composite rain-mass (M_w) distribution at 3.5-km height. The M_w was derived from Z and $Z_{\rm DR}$ with the relationship by Cifelli et al. (2002) as

$$M_w = 0.7x10^{-3} Z^{0.886} \left(10^{\frac{Z_{DR}}{10}}\right)^{-4.159}. \quad (6)$$

It is clear in Figure 3b that the M_w at 3.5-km level increased non-linearly with d_{obs}, and the normalized frequency distribution for M_w rose rapidly for objects with d_{obs} of 0–8 km. For objects with d_{obs}>8 km, the increase rate of M_w was more gradual than that for objects with d_{obs}<8 km. Compared to the ETH distribution in Figure 3a, the M_w distribution at 3.5-km level is narrower at higher M_w values, suggesting less case-dependent variabilities.

To identify the type of precipitation which was most sensitive to the d_{obs}, the full statistical distributions between precipitation rates (R) and separation distance (d_{obs}) at 0.5-km height are shown in Figure 4. Precipitation rate (R) was derived at each radar gate with a blended algorithm that objectively chose different R estimations based on the magnitude of polarimetric variables (Cifelli et al., 2011; Thompson et al., 2018). Figure 4a shows that R changed little with the increasing d_{obs} at 25th percentile. A nonlinear increase in R with the increasing d_{obs} can be identified at larger percentiles (Figures 4b-d), however. At 75th percentile (Figure 4c), R rose at a rapid rate for d_{obs} of 0–8 km and rose at a more gradual rate for d_{obs}>8 km.

While the raindrops associated with mixed-phase and ice microphysics ("cold rain") cannot be directly distinguished from those associated with "warm rain" microphysics, the contribution of ice-phase microphysics to R likely peaks at or slightly beneath the melting level (Yang and Houze, 1995; Kain et al., 2000; Jensen et al., 2018). Thus, we inferred from Figure 3b that the ice-phase and mixed-phase microphysics (responsible for rain mass at 3.5-km height or 0.5 km below the 0°C level) could be critical in producing more M_w near large d_{obs} objects. The similarity between M_w and R distributions at high percentiles in Figures 4c and 4d also implies that the greater likelihood of intense precipitation near large d_{obs} objects could be attributable to the ice-phase and mixed-phase microphysical processes. These inferences will be discussed further with WRF simulation in Sections 5 and 6.

4. Simulation results of the 20 June 2015 MCS

4.1 MCS track and morphology

Figure 5 compares the temporal evolution of the vertical column-maximum radar reflectivity between the observation and WRF simulation from 0600 UTC to 1100 UTC on 20 June 2015. The observed MCS was initially located in central South Dakota at 0600 UTC and propagated eastward in the next five hours. The observed movement of this MCS (Figures 5f-j) was reproduced reasonably well by the WRF simulation (Figures 5a-e). Both the simulated and observed MCSs belonged to the MCS archetype with leading-line and trailing-stratiform (LLTS) characteristics (e.g., Houze et al., 1989; Parker and Johnson, 2000). There were certain times when the observed and simulated MCSs were structurally different. For example, the observed MCS at 0600 UTC (Figure 5f) consisted of a bow echo and two secondary convective lines at the northeast and southwest of the

bow echo. While the WRF produced a bow echo with similar orientation to the observed (Figure 5a), the simulated northeastern secondary line was less organized than the observed. The morphological differences disappeared by 0700 UTC (Figures 5b and 5g), as the simulated northeastern line grew upscale and merged with the bow echo. There were little morphological differences between the simulated and observed MCSs after 0700 UTC (comparing Figures 5c-e with Figures 5h-j).

4.2 Precipitation characteristics

To validate the MCS precipitation, we bilinearly interpolated the rainfall outputs from the WRF simulation and the National Stage-IV Quantitative Precipitation Estimation (QPE) Product (ST4) from the National Centers for Environmental Prediction (NCEP) onto the same rectilinear latitude-longitude grid with resolution of 0.025° by 0.025°. Precipitation grids within the domain from 105.5°W to 95°W and from 42.5°N to 46.5°N were used for the analyses. The domain was chosen to ensure that the analyses were representative of the main MCS on 20 June 2015.

The ST4 precipitation Hovmöller diagram in Fig. 6a shows an eastward-propagating precipitation feature from 0230 UTC to 0530 UTC. This feature stalled and expanded longitudinally from 0530 to 0700 UTC, both of which are related to the merger of secondary line with the main MCS. The precipitation feature resumed its eastward propagation trend after 0730 UTC, with an eastward jump in the mean precipitation location compared to the pre-stalling precipitation location. This "location jump" in mean precipitation location is similar to the "discrete propagation" phenomena documented by Fovell et al. (2006).

The Hovmöller diagram of the simulated precipitation in Fig. 6b shows a similar evolution to the observed in Fig. 6a from 0200 to 0530 UTC. Precipitation evolution analogous to the observed stalling and longitudinal expansion in the simulation occurred approximately one hour later than the observed. Despite the 1-h delay, the WRF simulation reproduced the "location jump" of the post-stalling precipitation feature. The main difference between the simulated and observed precipitation was that the WRF simulation lacked the secondary precipitation east of the main MCS. The most prominent feature of the secondary precipitation initiated near 96°W at 0600 UTC and merged into the main MCS at 1000 UTC (Fig. 6a). Reflectivity mosaic from the NEXRAD (not shown) indicated that the secondary feature was related to a small convective cluster displaced to the northeast of the main MCS from 0600 to 0900 UTC. The fact that the WRF simulation failed to develop this cluster might explain the lack of secondary features in Fig. 6b.

4.3 Convective echo structure

Figure 7 compares the contoured frequency by altitude diagrams (CFADs; Yuter and Houze, 1995a) of radar reflectivity (Z) over the convective regions during the mature and weakening phases of the MCS life cycle. To distinguish the

main MCS from isolated convection, a contour-finding technique was applied to the observed and simulated reflectivity fields at 2-km height. The largest contiguous area bounded by the 20-dBZ contour was defined as the main MCS. To facilitate the discussion on the temporal evolution of radar-echo structure, the analysis period of 0300–1200 UTC was separated into the developing, mature, and weakening phases, based on the time series of mean echo-top heights (ETHs) of 20 dBZ. Periods with increasing, steady, and decreasing ETHs were denoted as the developing (0300–0500 UTC), mature (0600–1000 UTC), and weakening phases (1000–1200 UTC), respectively. Perturbing the cutoff timing by ±1 hour did not affect the results substantially. Data from 0500 to 0600 UTC were not used because of inadequate radar-data coverage at lower levels.

The CFAD of observed Z in convective region during the mature phase (Figure 7a) contains three areas of interest. The first is the steady increase in Z with decreasing altitude beneath 4 km. The second is the Z increase with decreasing altitude between 4 km and 8 km. The third one is the modest decrease in Z above 8 km. The main difference of Z-CFAD between the observed (Figure 7a) and the simulated (Figure 7b) is the rapid decrease of Z above 8 km and the modest decrease of Z at 4–8 km in WRF simulation (see Table 3). This error resulted from an overestimation of Z by ~10 dBZ between 8 km and 10 km in the WRF. The overestimation of Z at upper levels (above 8 km in this case) is common for simulations of deep convective systems (e.g., Varble et al. 2011, 2014; Wu et al., 2013; Bodine and Rasmussen, 2017; Stanford et al. 2017). Despite this bias, the Z CFADs below 8 km from the simulation and observation were comparable. Specifically, the simulated change rates of Z beneath the melting level and 4–8 km were both within 20% of the observed values (Table 3).

As the observed MCS entered the weakening phase, reflectivity between 5 km and 8 km dropped by 5–10 dBZ compared to those at the mature phase, whereas a tendency of Z decrease with decreasing altitudes could be seen below 2 km (Figure 7c). Compared to the observation, the WRF overestimated reflectivity above 8 km and did not have a decrease in Z below 2 km (Figure 7d). On the other hand, the 5–10 dBZ reflectivity decrease at 4–8 km was reproduced in the simulation, however. The simulated change rate of Z at 4–8 km in the weakening phase was closer to the observed value, compared to other layers (Table 3).

4.4 Spatial correspondence between size-sorting signatures and low-level flow directions

To verify whether the WRF model produced size-sorting signatures or not, we compared the simulated D_{mr}-N_{Tr} distributions at the lowest model level at 0720 UTC (Figures 8d-f) to the observed Z_{DR}-K_{DP} distributions at 1-km height at 0620 UTC (Figures 8a-c). The timing difference was to account for the 1-h delay in the merger of secondary line with main MCS. Radial velocity measurements from two NEXRAD radars (KABR and KFSD) were used to retrieve ground-relative winds (u_g, v_g) and vertical wind (w). We then calculated the system-relative wind (u_r, v_r) by subtracting the MCS movement vector (u_{MCS}, v_{MCS})

from ground-relative wind. MCS movement was determined by tracking the movement of the centroids of the closed 20-dBZ contours from 0300 to 1200 UTC. The movement vector of the MCS (u_{MCS}, v_{MCS}) was determined to be (26.1, –1.35) m s^{-1} for the observed 20 June MCS, and (24.5, –1.67) m s^{-1} for the simulated MCS, respectively.

Figures 8b and 8c show that for the observed MCS, the enhancements in K_{DP} were located downwind of both the Z_{DR} enhancements and updrafts. The angle between Z_{DR} and K_{DP} enhancements roughly paralleled the system-relative inflow. These observed spatial patterns were reproduced in the WRF simulation (Figures 8d and 8f). For example, two areas with larger D_{mr} could be found near $X = 900$ km and $X = 913$ km, and downwind of these D_{mr} enhancements and updrafts were two isolated areas with enhanced N_{Tr} near $X = 885$ km and $X = 900$ km in Figure 8f.

5. Low-level size-sorting signatures of the 20 June 2015 MCS

5.1 Statistical relationship between convective height and separation distances

Bivariate distributions of ETH versus separation distance for the observed and simulated MCSs on 20 June 2015 are shown in Figures 9a and 9b, respectively. The ETH values for objects with smaller d_{WRF} identified in the simulated MCS (Figure 9b) were larger than the ETH values for corresponding smaller d_{obs} in the observed MCS (Figure 9a). Critical characteristics of the ETH-d_{obs} distribution of the observed 20 June MCS was retained in the WRF simulation, namely the shift towards higher ETHs with increasing d_{WRF} magnitudes (Figures 9a, 9b). This suggests that the WRF simulation could capture the main statistical correlation between the observed separation distances (d_{OBS}) and the ETHs.

5.2 Statistical relationship between separation distances and microphysical properties

Figure 9c shows the bivariate distribution of d_{WRF} versus ice/liquid water path (IWP/LWP). It is clear that the IWP distribution resembled the ETH distribution, but the LWP distribution did not resemble the ETH distribution. The normalized d_{WRF}−IWP bivariate frequency distribution (blue contours in Figure 9c) shifts to higher IWP magnitudes when d_{WRF} increases from 7.5 km to greater than 10 km**.** On the other hand, normalized d_{WRF}−LWP bivariate frequency distribution (orange contours in Figure 9c) shows no appreciable LWP trend with increasing d_{WRF} up to 11 km and trends slightly towards lower LWP magnitudes when d_{WRF} increases beyond 11 km.

A reasonable question to ask is whether or not the surface precipitation is also correlated to d_{WRF}. The simulated size-sorting objects were separated into three categories based on the ETH-d_{WRF} bivariate distribution (Figure 9b). The first category contained objects with $d_{\mathrm{WRF}} < 7.5$ km, the second category was for 7.5 km $< d_{\mathrm{WRF}} <$ 10.5 km objects, whereas the third category was for $d_{\mathrm{WRF}} >$ 10.5 km objects. The statistical distributions of R near size-sorting objects of the second and third categories (objects for 7.5 km $< d_{\mathrm{WRF}} <$ 10.5 km and

objects for $d_{\mathrm{WRF}} > 10.5$ km) during the MCS mature phase are compared in Figure 10. The statistical distributions of R for these two object categories were very similar for weaker precipitation rate ($R < 50$ mm h^{-1}). However, the large d_{WRF} objects were more likely to produce *intense* precipitation ($R > 100$ mm h^{-1}) than the moderate d_{WRF} objects.

Figure 9c shows that more ice and mixed phase hydrometeors were produced near the large d_{WRF} objects. The sedimentation and subsequent melting of these ice particles are hypothesized to contribute to the greater likelihood of intense rainfall near large $d_{\mathrm{obs}}/d_{\mathrm{WRF}}$ objects. We will evaluate this hypothesis with vertical profiles of different rain-mass components in Section 6.

5.3 Statistical relationship between separation distances and thermodynamic characteristics

In this subsection, the latent heating and cooling terms from WRF model were grouped into six essential microphysics components (deposition, freezing, condensation, sublimation, melting, and evaporation). To minimize uncertainties in the vertical, d_{WRF} were compared to the vertically-integrated values of each microphysics component.

Figures 11a-c show the bivariate distributions of three latent heating terms. Notice that the vertically-integrated latent heating and cooling terms in the y-axis in Figure 11 were displayed in their log values. The integrated condensation heating rates ($\int P_{\mathrm{Cond}}$; Figure 11c) were half an order magnitude higher than the deposition rates ($\int P_{\mathrm{Dep}}$; Figure 11a), and an order magnitude higher than the freezing rates ($\int P_{\mathrm{Frz}}$; Figure 11b), respectively. The dominant role of condensation in the convective regions is consistent with simulations on two MCSs during the Midlatitude Continental Convective Clouds Experiment (MC3E; Jensen et al. 2016) by Marinescu et al. (2016). The $\int P_{\mathrm{Cond}}$ and $\int P_{\mathrm{Dep}}$ were insensitive to separation distance (d_{WRF}), with most size-sorting objects having very similar integrated condensation and deposition rates aloft (Figures 11a and 11c). In contrast, the distance of $\int P_{\mathrm{Frz}}$ (Figure 11b) was similar to the ETH and IWP distributions (Figures 9b and 9c) in showing a nonlinear relationship with the separation distance (d_{WRF}), with higher (lower) $\int P_{\mathrm{Frz}}$ near large (small) d_{WRF} objects.

The distributions of three latent cooling terms are shown in Figures 11d-f. Both vertically-integrated sublimation ($\int P_{\mathrm{Sub}}$; Figure 11d) and melting ($\int P_{\mathrm{Melt}}$; Figure 11e) became more negative or stronger with d_{WRF}. In particular, the shape of the $\int P_{\mathrm{Melt}}$ versus d_{WRF} distribution was similar to those of the ETH, IWC, and $\int P_{\mathrm{Frz}}$ but inverted. In contrast, we find very similar $\int P_{\mathrm{Evap}}$ distribution for objects with different d_{WRF} values (Figure 11f), suggesting that total evaporative cooling was insensitive to d_{WRF}.

The similarity between the $\int P_{\mathrm{Frz}}$ and $\int P_{\mathrm{Melt}}$ distributions to those of the ETH and IWP supports our findings in Section 4b in showing that enhanced ice/mixed phase processes near large d_{WRF} objects. Thus, we can infer from

Figure 11 that the integrated latent heat release of freezing and the latent heat absorption of melting vary with d_{WRF}. On the other hand, the integrated latent heat release of condensation and deposition and latent heat absorption of evaporation are invariant to d_{WRF}.

5.4 Statistical differences in thermodynamic profiles

While bivariate distributions in Figure 11 elucidated some statistical relationships between local thermodynamics and separation distance (d_{WRF}), some ambiguities still remain. Detailed information in the vertical is lost in the vertical integration. This produces some uncertainties to the interpretation of flat bivariate distributions in Figures 11a and 11c.

Differences in statistical characteristics in the vertical are illustrated in this section with CFAD differences between objects of the second and third ETH-d_{WRF} categories used (Figure 9b). The signs of the contours on the right-hand side (RHS) of the CFAD difference figures (Figures 9–14) are critical to the interpretation herein. Since CFADS show how the probability distributions of a physical variable evolve in the vertical, positive (negative) difference on the RHS of Figures 9–14 implies that the magnitudes of the variable will be larger near the larger (smaller) d_{WRF} objects.

Since the CFAD differences figures are noisy, we used the Kolmogorov-Smirnov two-sample test (K-S test; Kolmogorov 1933; Smirnov 1939; Massey 1951) to identify the temperature levels where the CFAD differences are statistically significant. The K-S test is a non-parametric test that determines if two samples have the same underlying distribution. The null hypothesis that the two samples are taken from the same statistical distribution is rejected with p-values less than 0.05. The CFAD differences at different temperature levels were deemed not statistically significant if the K-S p-values were greater than 0.05. The same statistical method was adopted by Stechman et al. (2020b) to discuss the differences between airborne in-situ microphysical measurements gathered in the transition zones and stratiform regions of different PECAN MCSs.

Figure 12 shows the CFAD differences for the freezing and melting terms, which are nonlinearly related to d_{WRF} when vertically integrated (Figures 11b and 11e). The temperature ranges where the CFAD differences were statistically significant are between –25°C and –15°C for freezing, and between 2°C and 15°C for melting. Within these temperature ranges, there were stronger freezing and cooling near the large d_{WRF} objects.

For other four latent heating or cooling terms (deposition heating, condensation heating, sublimation cooling, and evaporation cooling) in Figure 13, CFAD differences at different temperature ranges roughly offset each other when vertically integrated. The following differences were shown to be statistically significant:

- Stronger evaporation near the large d_{WRF} objects within the temperature ranges between 0°C and 8°C and between 15°C and 20°C (Figure 13d).

- Stronger sublimation near the large d_{WRF} objects from –2°C to 5°C (Figure 13c).
- Weaker deposition near the large d_{WRF} objects within temperature range from –5°C to –25°C, and weaker condensation near the large d_{WRF} objects within temperature range from 0°C to 8°C (Figures 13a and 13b).

5.5 Implications of the thermodynamic variabilities on kinematics

While ETH reveals correlation between convective kinematics and separation distance (d_{WRF}), two questions remained unanswered. Firstly, are the deeper echoes near large d_{WRF} objects mostly tied to updrafts at lower, middle, or upper levels? Secondly, is the correlation statistically significant? Vertical motion (w) in updrafts is determined by the buoyancy and pressure gradient force (Peters, 2016). While latent heat release during phase change can make the air parcel more buoyant, whether the increased buoyancy translates to stronger w is dependent upon updraft slopes (Parker, 2010) and widths (Morrison, 2016; Peters, 2016). Furthermore, other factors like hydrometeor loading and entrainment can also impact w (e.g., Tao et al., 1995; Storer and van den Heever, 2013).

Figure 14 shows the difference between the updraft and downdraft CFADs of the two object categories. Stronger updrafts above (beneath) the melting level for the larger (smaller) d_{WRF} objects are shown in Figure 14a. Downdrafts beneath the melting level were slightly stronger near large d_{WRF} objects than those near smaller d_{WRF} objects (Figure 14b).

Many of these kinematic differences are either marginally above or below the K-S significance threshold. This was particularly true for downdrafts, for which the p-values were mostly greater than 0.05 (Figure 14b). On the other hand, there were more temperature ranges where the CFAD differences in updrafts were statistically significant (Figure 14a). One of these temperature ranges was between –13°C and –20°C, which matched the freezing enhancement shown in Figure 12a.

5.6 Spatial similarities between graupel sedimentation patterns and size sorting signatures

Apart from the magnitudes of different variables, it is also important to understand how hydrometeor DSD variables distribute near size-sorting objects. Figure 15 shows the mean spatial distributions of D_{mr} and N_{Tr} within the 12 km diameter circles collocated to all identified simulated size-sorting objects at 0.25-km height and 4-km height, respectively. Spatial distributions corresponding to each object were first interpolated to the polar coordinate and rotated so that the wind directions within the 12 km diameter circle were fixed easterly. The composited D_{mr} at 0.25 km was located in the upwind (i.e., right-hand) side of Figure 15d, whereas 0.25-km N_{Tr} was located in the downwind (i.e., left-hand) side of Figure 15e. Figures 15a-c show the mean distributions of graupel diameter (D_{mg}; Figure 15a), number concentration (N_{Tg}; Figure 15b), and w at

4-km height (Figure 15c). A clear spatial separation between D_{mg} and N_{Tg} can be observed. Larger, but less numerous, graupel particles were distributed in the upwind side and were fairly close to the strongest updrafts. In contrast, smaller, but more numerous, graupel were located in the downwind side of Figure 15b.

When we compare the graupel and rain DSD distributions in polar coordinates, it is clear that the D_{mr} and D_{mg} distributions were rather similar. On the other hand, N_{Tr} distribution maxima were located slightly upwind of the N_{Tg} maxima. Raindrops originated from graupel particles advected further downwind are small and may evaporate before reaching the surface, which could explain the slight spatial displacement between N_{Tr} and N_{Tg} maximum. In any case, Figure 15 provides the evidence on the role of graupel sedimentation in generating size-sorting signatures. It also suggests that the production and fallout of a small quantity of large graupel particles was critical in spatially separating D_{mr} from N_{Tr}.

6. Discussion

Based on the "particle fountain" model (Yuter and Houze, 1995b; Zeng et al., 2001), we originally hypothesized that areas with larger (smaller) $d_{\rm obs}/d_{\rm WRF}$ at the lower levels would coincide with greater (less) ice DSD spatial separation aloft and stronger (weaker) updrafts.

The statistical analyses suggested a more ambiguous relationship between size sorting and convective kinematics than the "particle fountain" model originally hypothesized. While the ETH generally increases with $d_{\rm obs}/d_{\rm WRF}$ (Figures 3a, 9a, and 9b), the $d_{\rm obs}/d_{\rm WRF}$ magnitudes over the places where this increase occur and the ETH increase rates are case-dependent. Thus, it would be difficult to use $d_{\rm obs}/d_{\rm WRF}$ *independently* to diagnose convective kinematics.

The separation distances ($d_{\rm obs}/d_{\rm WRF}$) are shown to be useful in diagnosing other convective properties. Statistical analysis on the PECAN MCSs revealed a clear tendency for more liquid water mass near the melting level for larger $d_{\rm obs}$ objects (Figure 3b). The WRF simulation results support this observational finding by showing more integrated freezing and melting for larger $d_{\rm WRF}$ objects (Figures 11b and 11e). Since the CFAD difference of deposition (Figure 13a) was close to the CFAD difference of freezing (Figure 12a) between –5°C and –25°C, this enhanced freezing likely occurred at the expense of deposition. The CFAD difference also showed more vapor condensation above the melting level for larger $d_{\rm WRF}$ objects than that near smaller $d_{\rm WRF}$ objects (Figure 13b).

Based on these analyses, a microphysical framework was proposed to interpret these findings. For the large $d_{\rm WRF}$ objects,

- More raindrops and water vapor were lifted to upper levels with subfreezing temperatures. Increase availability of supercooled liquid made it easier for graupel particles to grow by collecting supercooled liquid droplets (riming process; Figures 11b and 12a).

- The sedimentation of heavier graupel particles enhanced the melting cooling (Figures 11e and 12b).

  On the other hand, for the smaller d_{WRF} objects,

- Most raindrops and water vapor stayed in vertical levels with warm temperatures, which reduced freezing heating aloft (Figure 12a).
- Deposition became the dominant ice generation mechanism in subfreezing temperatures (Figures 11a, 11b, and 13a).
- Ice hydrometeors formed aloft were lighter and less likely to fall to lower levels with warmer temperatures and melt (Figures 11e and 12b).

These microphysical and thermodynamic processes have important implications on the dominant precipitation pathways associated with different size-sorting object categories. Figure 16a compares the 95-percentile vertical profiles of rain mass generated through the warm pathway (q_{Warm}) and the cold pathway (q_{Melt}). Partition of rain mass through the warm and cold pathways follows this equation,

$$\begin{cases} q_{\mathrm{Warm}} = q_{r\_ac} + q_{r\_cn} + q_{r\_cond}, & (7a) \\ q_{\mathrm{Melt}} = q_{g\_mlt} + q_{s\_mlt} + q_{i\_mlt}, & (7b) \end{cases}$$

where q_{Warm} is the sum of rain mass generated through accretion (q_{r_ac}), autoconversion (q_{r_cn}), and vapor condensation (q_{r_cond}), whereas q_{Melt} is the sum of rain mass generated from melted graupel (q_{g_mlt}), melted snow (q_{s_mlt}), and melted ice (q_{i_mlt}). Figure 16a compares the 95^{th} percentile q_{Warm} and q_{Melt} vertical profiles for large d_{WRF} objects (black lines) and smaller d_{WRF} objects (red lines). More q_{Melt} was produced near the large d_{WRF} objects, whereas more q_{Warm} was produced near the smaller d_{WRF} objects, which agrees with the proposed microphysical framework. The CFAD differences for the graupel number concentration and snow concentration suggest that the enhanced q_{Melt} was largely related to increased graupel fallout to levels with warmer temperatures (not shown). Based on these findings, it was concluded that d_{WRF} could potentially be used to diagnose the amount of rain mass generated via the cold pathway relative to that generated via the warm pathway. A schematic diagram of the microphysical processes leading to different d_{obs}/d_{WRF} is shown in Figure 17.

Finally, the CFAD differences in evaporative and sublimation cooling *magnitudes* between larger d_{WRF} objects and smaller objects (Figures 13c and 13d) indicate a greater likelihood for larger d_{WRF} objects to have stronger evaporative and sublimation cooling at or slightly beneath the melting level. A possible explanation for this is local enhancements in rear inflow jets (RIJs; Yang and Houze, 1995; Grim et al., 2009). Since graupel particles experienced more advection in stronger updrafts, graupel particles formed near large d_{WRF} objects were more likely to sublimate in the drier air behind updrafts (Figure 16b).

While there were no in-situ measurements within the convective region of the 20 June MCS, a spiral profile taken in its transition zone did show signs of active sublimation near a strong RIJ (Stechman et al., 2020a; see their Figure 22).

7. Conclusions

This study evaluates the feasibility of using $d_{\mathrm{WRF}}/d_{\mathrm{obs}}$ to infer convective variabilities in nocturnal MCSs during the PECAN field campaign. An object-based method was used to identify a large quantity of size-sorting signatures in the convective regions of 10 nocturnal MCSs. Local kinematic, microphysical, and thermodynamic characteristics were then extracted for each object and compared to its separation distance.

We have listed three scientific questions related to hydrometeor size sorting in the Introduction Section. We will now examine if these questions are addressed with the analysis presented. Bivariate statistics show a positive correlation between separation distance ($d_{\mathrm{obs}}/d_{\mathrm{WRF}}$) and echo-top height (ETH; Figures 3a, 9a, and 9b). Although Figure 14a shows positive updraft CFAD difference between large d_{WRF} objects and smaller d_{WRF} objects, the statistical difference is mostly statistically insignificant. Thus, we conclude that size sorting objects' magnitudes have positive but statistically insignificant correlations to the convective updraft intensities.

Statistically significant differences in thermodynamics and the precipitation pathways were found for objects with different separation distance (d_{WRF}; Figures 11, 12, 13, and 16a). Similarities in the nonlinear correlations between the ETH, IWP, integrated freezing heating, and integrated melting cooling (Figures 9b, 9c, 11b, and 11e) suggest that changes in convective depth with separation distance can mostly be attributed to the latent heat released through the riming process.

Taking all results presented in Section 5 into account, we find that the separation distance (d_{WRF}) can potentially be used to diagnose contributions from riming heating and melting cooling to the overall convective thermodynamic structure (Figures 11b, 11e, and 12). Additionally, separation distance may reveal some information whether convective heating above melting level is more dominated by deposition or riming (Figures 12a and 13a). More riming growth of graupel particles near large d_{WRF} objects caused the local dominant precipitation pathway to shift more towards the cold pathway (Figure 16a). Statistical analysis on precipitation characteristics (Figures 4 and 10) suggest that increased rain mass generated through the cold pathway near the large d_{WRF} objects contributed to the greater likelihood of intense precipitation. For the smaller d_{WRF} objects, reduced rain production from the cold pathway was partially compensated by warm rain production.

In short, separation distances were shown to be related to different convective variabilities. The most critical factor leading to this correlation is the production and subsequent fallout of large graupel particles. Convective areas would have larger separation distances if there were larger graupel particles in these areas

and fell in close vicinity to the updrafts. The correlation between separation distances and graupel growth also indicates that the separation distances can be used to infer the thermodynamic characteristics near and above the melting level.

This study builds upon previous modeling studies that examined different factors leading to the observed polarimetric signatures (e.g., Kumjian et al., 2014; Dawson et al., 2014; Snyder et al., 2017; Ilotoviz et al., 2018). These results provided practical guidance on various variabilities near size-sorting signatures of different magnitudes. From a modeling perspective, our results suggest that separation distances can be used to evaluate different microphysical assumptions used in models. For example, the temporal evolution of separation distances can be used to quantify how microphysical assumptions impact the spatial variabilities of drop-size distributions of ice hydrometeors aloft and how these DSD variabilities affect the MCS dynamics.

Finally, while our results are based upon statistical analyses on a large dataset from 10 MCSs during PECAN experiments, uncertainties still remain as to the general applicability of our conclusions, especially for those related to the precipitation pathways. The cold pathway was more important than the warm pathway in generating *intense* precipitation in MCSs during PECAN. However, warm pathway may be more important in producing rainfall for MCSs occurring in other environments. A climatological analysis on the size-sorting signatures in MCSs over a wide range of geographical locations and seasons is needed to verify our conclusions. Another limitation in this study is that we have not discussed the interaction between convective drafts and ambient environments. More work is needed to clarify the kinematic variability, possibly through re-classifying size-sorting objects based on updraft width/slope or environmental shear/instability magnitudes. The other limitation is the instantaneous nature of the existing algorithm, which could bias our results against slow-occurring processes. It is also difficult to use the current algorithm to investigate the linkage between separation distances and the life cycle of individual convective elements. Future work should address these limitations by using convection-tracking technique to trace the temporal evolution of different size-sorting objects.

Acknowledgements

The authors would like to thank Profs. Ben Jong-Dao Jou and Jen-Ping Chen for their helpful suggestions to this study. The authors would also like to thank Mr. Jyong-En Miao and Mr. Yao-Chu Wu for providing support on modeling and data visualization. Finally, the authors would like to thank the many PECAN participants for their hard work in obtaining the observational data. The radar observations analyzed in this study can be obtained from the archival website (ncei.noaa.gov/access/search/data-search/weather-radar-level-ii) hosted by the National Centers for Environmental Information (NCEI). The WRF model used in the simulation is available online at github.com/NCAR/WRFV3. This work is supported by the Ministry of Science and Technology of Taiwan under Grant MOST 107-2111-M-002-013

and MOST 108-2111-M-002-011-MY2. Data used in this study are available from the corresponding author (mingjen@as.ntu.edu.tw) upon reason request.

APPENDIX

Are the statistical relationships sensitive to model horizontal resolution?

It is possible that the coarser resolution used in this study (a horizontal grid size of 3 km) might not properly represent the size-sorting feature, which is fundamentally a convective-scale process. However, it is evident in Figure A1 that the simulation with a grid size of 3 km can still replicate the *net effect* of the size-sorting phenomenon on spatial distribution and local variability of hydrometeors.

Figure A1 shows the mean spatial distributions of D_{mg} and N_{Tg} at 4-km height from the simulation which has the same model configuration in Table 2 except with 1-km horizontal grid size. It is clear from Figure A1b that more N_{Tg} were produced and advected rearward from the 1-km simuation, compared to those from 3-km simulation (Figure 15b). The N_{Tg} also tended more to concentrate in the second quadrant from 1-km run. However, both experiments show a similar spatial trend that D_{mg} leads N_{Tg} (see Figures 15a,b and Figure A1a,b) The statistical distributions between the echo-top height (ETH), the freezing heating, and the separation distances from 1-km simulation (Figures A1c and A1d) were generally similar to those from the 3-km simulation (Figures 9b and 11b). Thus, this comparison indicates that although individual convective drafts cannot be well resolved by the simulation with 3-km grid spacing, the 3-km simulation can still capture *the net effect of several drafts in close proximity on hydrometeor DSD, local kinematics, and local thermodynamics.*

References

Bodine, D. J., & Rasmussen., K. L. (2017). Evolution of mesoscale convective system organizational structure and convective line propagation. *Monthly Weather Review*, **145 (9)**, 3419–3440. https://doi.org/10.1175/MWR-D-16-0406.1.

Braun, S. A., & Houze, R. A. Jr. (1996). The heat budget of a midlatitude squall line and impli-483cations for potential vorticity production. *Journal of the Atmospheric Sciences*, **53 (9)**, 1217–1240. https://doi.org/10.4841175/1520-0469(1996)053 1217:THBOAM 2.0.CO;2.

Cifelli, R., Chandrasekar, V., Lim, S., Kennedy, P. C., Wang, Y., & Rutledge, S. A. (2011). A new dual-polarization radar rainfall algorithm: Application in Colorado precipitation events. *Journal of Atmospheric and Oceanic Technology*, **28 (3)**, 352–364. https://doi.org/10.1175/4882010JTECHA1488.1.

Cifelli, R., Petersen, W. A., Carey, L. D., Rutledge, S. A., & da Silva Dias, M. A. F. (2002). Radar observations of the kinematic, microphysical, and precipitation characteristics of two MCSs in TRMM-LBA. *Journal of Geophysical*

Research, **107 (D20)**, LBA 44–1–LBA 44–16. https://doi.org/10.4921029/2000JD000264.

Dawson, D. T. II, Xue, M., Milbrandt, J. A., & Yau, M. K. (2010). Comparison of evaporation and cold pool development between single-moment and multimoment bulk microphysics schemes in idealized simulations of tornadic thunderstorms. *Monthly Weather Review*,**138 (4)**, 1152–1171. https://doi.org/10.1175/2009MWR2956.1.

Dawson, D. T. II, Mansell, E. R., Jung, Y., Wicker, L. J., Kumjian, M. R., & Xue, M. (2014). Low-level Zdr signatures in supercell forward flanks: The role of size sorting and melting of hail. *Journal of Atmospheric Sciences*, **71 (1)**, 276–299. https://doi.org/10.1175/JAS-D-13-0118.1.

Dawson, D. T. II, Mansell, E. R., & Kumjian, M. R. (2015). Does wind shear cause hydrometeor size sorting? *Journal of Atmospheric Sciences*, **72 (1)**, 340–348. https://doi.org/10.1175/JAS-D-14-0084.1.

Didlake, A. C., & Kumjian, M. R. (2018). Examining storm asymmetries in Hurricane Irma (2017) using polarimetric radar observations. *Geophysical Research Letter.*, **45**, 13,513–13,522. https://doi.org/10.1029/2018GL080739.

Dudhia, J. (1989). Numerical study of convection observed during the winter monsoon experiment using a mesoscale two–dimensional model. *Journal of Atmospheric Sciences*, **46**, 3077–3107. https://doi.org/10.1175/1520-0469(1989)046 3077:NSOCOD 2.0.CO;2.

Feng, Y., & Bell, M. (2018). Microphysical characteristics of an asymmetric eyewall in major hurricane Harvey. *Geophysical Research Letter*, **46**, 461– 471. https://doi.org/10.1029/2018GL080770.

Fovell, R. G., Mullendore, G. L., & Kim, S.-H. (2006). Discrete propagation in numerically simulated nocturnal squall lines. *Monthly Weather Review*, **134 (12)**, 3735–3752, https://doi.org/10.1175/498MWR3268.1.

Gabella, M., & Notarpietro, R. (2002). Ground clutter characterization and elimination in mountainous terrain. *Copernicus GmbH*, 305–311.

Gallus, W. A. Jr., & Johnson, R. H. (1991). Heat and moisture budgets of an intense midlatitude squall line. *Journal of Atmospheric Sciences*, **48 (1)**, 122–146. https://doi.org/10.1175/1520-0469(1991)048 0122:503HAMBOA 2.0.CO;2.

Geerts, B., & Coauthors. (2017). The 2015 plains elevated convection at night field project. *Bulletin of American Meteorological Society,* **98 (4)**, 767–786. https://doi.org/10.1175/BAMS-D-15-00257.1.

Grim, J. A., Rauber, R. M., McFarquhar, G. M., Jewett, B. F., & Jorgensen, D. P. (2009). Development and forcing of the rear inflow jet in a rapidly developing and decaying squall line during BAMEX. *Monthly Weather Review*, **137 (4)**, 1206–1229. https://doi.org/10.1175/2008MWR2503.1.

Helmus, J., & Collis, S. (2016). The Python ARM Radar Toolkit (Py-ART), a library for working with weather radar data in the Python programming language. *Journal of Open Research Software*, **5114 (1)**, p.e25. http://doi.org/10.5334/jors.119.

Homeyer, C. R., & Kumjian, M. R. (2014). Microphysical characteristics of overshooting convection from polarimetric radar observations. *Journal of Atmospheric Sciences*, **72 (2)**, 870–891. https://doi.org/10.1175/JAS-D-13-0388.1.

Houze, R. A. Jr., Biggerstaff, M. I., Rutledge, S. A., & Smull, B. F. (1989). Interpretation of Doppler weather radar displays of mid-latitude mesoscale convective systems. *Bulletin of American Meteorological Society*, **70 (9)**, 608–619. https://doi.org/10.1175/1520-0477(1989)070 0608:IODWRD 2.0.515CO;2.

lotoviz, E., Khain. A., Ryzhkov, A. V., & Snyder, J. C. (2018). Relationship between aerosols, hail microphysics, and ZDR columns. *Journal of Atmospheric Sciences*, **75 (6)**, 1755–1781, https://doi.org/10.1175/JAS-D-17-0127.1.

Janjic, Z. I. (1994). The step-mountain eta coordinate model: Further developments of the convection, viscous sublayer, and turbulence closure schemes. *Monthly Weather Review*, **122 (5)**, 927–945. https://doi.org/10.1175/1520-0493(1994)122 0927:TSMECM 2.0.CO;2.

Jensen, A. A., Harrington, J. Y., & Morrison, H. (2018). Microphysical characteristics of squall-line stratiform precipitation and transition zones simulated using an ice particle property-evolving model. *Monthly Weather Review*, **146 (3)**, 723–743. https://doi.org/10.1175/MWR-D-17-0215.1.

Jensen, M. P., & Coauthors. (2016). The Midlatitude Continental Convective Clouds Ex-periment (MC3E). *Bulletin of American Meteorological Society*, **97 (9)**, 1667–1686, https://doi.org/10.1175/BAMS-D-14-00228.1.

Kain, J. S. (2004). The Kain–Fritsch convective parameterization: An update. *Journal of Applied Meteorology*, **43**,170–181. https://doi.org/10.1175/1520-0450(2004)043 0170:TKCPAU 2.0.CO;2.

Kain, J. S., Goss, S. M., and Baldwin, M. E.. (2000). The melting effect as a factor in precipitation-type forecasting. *Weather Forecasting*, **15 (6)**, 700–714. https://doi.org/10.1175/1520-0434(2000)015 0700:TMEAAF 2.0.CO;2.

Kolmogorov, A. (1933). Sulla determinazione empirica di una legge di distributione. *Giornale dell'Istituto Italiano degli Attuari*, **4**, 1–11.

Kumjian, M. R., & Ryzhkov, A. V. (2008). Polarimetric signatures in supercell thunderstorms. *Journal of Applied Meteorology and Climatology*, **47 (7)**, 1940–1961. https://doi.org/10.1175/2007JAMC1874.1.

Kumjian, M. R., & Ryzhkov, A. V. (2012). The impact of size sorting on the polarimetric radar variables. *Journal of Atmospheric Sciences*, **69 (6)**, 2042–2060. https://doi.org/10.1175/JAS-D-11-0125.1.

Kumjian, M. R., Khain, A. P., Benmoshe, N., Ilotoviz, E., Ryzhkov, A. V., & Phillips., V. T. J. (2014). The anatomy and physics of Zdr columns: Investigating a polarimetric radar signature with a spectral bin microphysical model. *Journal of Applied Meteorology and Climatology*, **53 (7)**, 1820–1843. https://doi.org/10.1175/JAMC-D-13-0354.1.

Lang, T. J., Ahijevych, D. A., Nesbitt, S. W., Carbone, R. E., Rutledge, S. A., & Cifelli, R. (2007). Radar-observed characteristics of precipitating systems during NAME 2004. *Journal of Climate*, **20 (9)**, 1713–1733. https://doi.org/10.1175/JCLI4082.1.

Laurencin, C. N., Didlake, A. C., Loeffler, S. D., Kumjian, M. R., & Heymsfield, G. M. (2020). Hydrometeor size sorting in the asymmetric eyewall of Hurricane Matthew (2016). *Journal of Geophysical Research, [Atmospheres]*, **125 (e2020JD032671)**, https://doi.org/10.1029/2020JD032671.

Lasher-Trapp, S., Kumar, S., Moser, D. H., Blyth, A. M., French, J. R., Jackson, R. C., Leon, D. C., & Plummer, D. M. (2018). On different microphysical pathways to convective rainfall. *Journal of Applied Meteorology and Climatology*, **57 (10)**, 2399–2417. https://doi.org/10.1175/JAMC-D-18-0041.1.

Loeffler, S. D., & Kumjian, M. R. (2018). Quantifying the separation of enhanced Zdr and Kdp regions in nonsupercell tornadic storms. *Weather Forecasting*, **33 (5)**, 1143 – 1157. https://doi.org/10.1175/WAF-D-18-0011.1.

Loeffler, S. D., Kumjian, M. R., Jurewicz, M., & French, M. M. (2020). Differentiating between tornadic and nontornadic supercells using polarimetric radar signatures of hydrometeor size sorting. *Geophysical Research Letter*, **47 (12)**, e2020GL088 242. https://doi.org/10.1029/2020GL088242.

Mansell, E. R., Ziegler, C. L., & Bruning, E. C. (2010). Simulated electrification of a small thunderstorm with two-moment bulk microphysics. *Journal of Atmospheric Sciences*, **67 (1)**, 171–194. https://doi.org/10.1175/2009JAS2965.1.

Marinescu, P. J., van den Heever, S. C., Saleeby, S. M., and Kreidenweis, S. M. (2016). The microphysical contributions to and evolution of latent heating profiles in two MC3E MCSs. *Journal of Geophysical Research, [Atmospheres]*, **121**, 7913–7935. https://doi.org/10.1002/2016JD024762.

Martinaitis, S. M. (2017). Radar observations of tornado-warned convection associated with tropical cyclones over Florida. *Weather Forecasting*, **32 (1)**, 165–186. https://doi.org/10.1175/WAF-D-16-0105.1.

Massey, J., F. J. (1951). The Kolmogorov-Smirnov test for goodness of fit. *Journal of the American Statistical Association*, **46 (253)**, 68–78. https://doi.org/10.1080/01621459.1951.10500769.

Mesinger, F., & Coauthors. (2006). North American Regional Reanalysis. *Bulletin of American Meteorological Society*, **87 (3)**, 343–360. https://doi.org/10.1175/BAMS-87-3-343.

Mlawer, E. J., Taubman, S. J., Brown, P. D., Iacono, M. J., & Clough, S. A. (1997). Radiative transfer for inhomogeneous atmospheres: RRTM, a validated correlated-k model for the longwave. *Journal of Geophysical Research*, **102 (D14)**, 16 663–16 682. https://doi.org/10.1029/97JD00237.

Morrison, H., Tessendorf, S. A., Ikeda, K., & Thompson, G. (2012). Sensitivity of a simulated midlatitude squall line to parameterization of raindrop breakup. *Monthly Weather Review*, **140 (8)**, 2437-2460. https://doi.org/10.1175/MWR-D-11-00283.1.

Morrison, H. (2016). Impacts of updraft size and dimensionality on the perturbation pressure and vertical velocity in cumulus convection. Part II: Comparison of theoretical and numerical solutions and fully dynamical simulations. *Journal of Atmospheric Sciences*, **73 (4)**, 1455–1480. https://doi.org/10.1175/JAS-D-15-0041.1.

Parker, M. D. (2010). Relationship between system slope and updraft intensity in squall lines. *Monthly Weather Review*, **138 (9)**, 3572–3578. https://doi.org/10.1175/2010MWR3441.1.

Parker, M. D., & Johnson, R. H. (2000). Organizational modes of midlatitude mesoscale convective systems. *Monthly Weather Review*, **128**, 3413–3436. https://doi.org/10.1175/1520-0493(2001)129 3413:OMOMMC 2.0.CO;2.

Peters, J. M. (2016). The impact of effective buoyancy and dynamic pressure forcing on vertical velocities within two-dimensional updrafts. *Journal of Atmospheric Sciences*, **73 (11)**, 4531–4551. https://doi.org/10.1175/JAS-D-16-0016.1.

Planche, C., Tridon, F., Banson, S., Thompson, G., Monier, M., Battaglia, A., & Wobrock, W. (2019). On the realism of the rain microphysics representation of a squall line in the WRF model. Part II: Sensitivity studies on the rain drop size distributions. *Monthly Weather Review*,**147 (8)**, 2811–2825. https://doi.org/10.1175/MWR-D-18-0019.1.

Rauber, R. M., & Nesbitt, S. W. (2018). *Radar Meteorology: A First Course.* Wiley-Blackwell, 488 pp.

Ryzhkov, A. V., & Zrnic, D. S.. (1998). Discrimination between rain and snow with a polarimetric radar. *Journal of Applied Meteorology*, **37 (10)**, 1228–1240. https://doi.org/10.1175/1520-0450(1998)037 1228:DBRASW 2.0.CO;2.

Skamarock, W., Klemp, J., Dudhia, J., Gill, D., Barker, D., Wang, W., & Powers, J. (2008). A description of the advanced research WRF, version 3.27, 3–27. *NCAR Tech.* Note NCAR/ TN-4751STR, 113 pp.

Smirnov, H. (1939). Sur les écarts de la courbe de distribution empirique. *Recueil Mathématique (Matemnticeskii Sbornik)*, **N.S. 6**, 3–26.

Snyder, J. C., Bluestein, H. B., Dawson, D. T. II, & Jung, Y. (2017). Simulations of polarimetric, X-band radar signatures in supercells. Part II: Zdr

columns and rings and Kdp columns. *Journal of Applied Meteorology and Climatology*, **56 (7)**, 2001–2026. https://doi.org/10.1175/JAMC-D-16-0139.1.

Stanford, M. W., Varble, A., Zipser, E., Strapp, J. W., Leroy, D., Schwarzenboeck, A., Potts, R., & Protat, A. (2017). A ubiquitous ice size bias in simulations of tropical deep convection. *Atmospheric Chemistry and Physics*, **17 (15)**, 9599–9621, https://doi.org/10.5194/acp-17-9599-2017.

Stechman, D. M., McFarquhar, G. M., Rauber, R. M., Bell, M. M., Jewett, B. F., & Martinez, J. (2020a). Spatiotemporal evolution of the microphysical and thermodynamic characteristics of the 20 June 2015 PECAN MCS. *Monthly Weather Review*, **148 (4)**, 1363–1388. https://doi.org/10.1175/586MWR-D-19-0293.1.

Stechman, D. M., McFarquhar, G. M., Rauber, R. M., Jewett, B. F., & Black, R. A. (2020b). Composite in situ microphysical analysis of all spiral vertical profiles executed within BAMEX and PECAN mesoscale convective systems. *Journal of Atmospheric Sciences*, **77 (7)**, 2541–2565. https://doi.org/10.1175/JAS-D-19-0317.1.

Steiner, M., Houze, R. A. Jr., & Yuter, S. E. (1995). Climatological characterization of three-dimensional storm structure from operational radar and rain gauge data. *Journal of Applied Meteorology and Climatology*, **34 (9)**, 1978–2007. https://doi.org/10.1175/1520-0450(1995)034 1978:CCOTDS 2.0.CO;2.

Storer, R. L., & van den Heever, S. C. (2013). Microphysical processes evident in aerosol forcing of tropical deep convective clouds. *Journal of Atmospheric Sciences*, **70 (2)**, 430–446. https://doi.org/10.1175/JAS-D-12-076.1.

Tewari, M., Chen, F., Wang, W., Dudhia, J., LeMone, M. A., Mitchell, K., Ek, M., Gayno, G., Wegiel, J., & Cuenca, R. H. (2004). Implementation and verification of the unified NOAH land surface model in the WRF model. *20th Conference on Weather Analysis and Forecasting/16th Conference on Numerical Weather Prediction*, pp. 11–15.

Tao, W.-K., Scala, J., & Simpson, J. (1995). The effects of melting processes on the development of a tropical and a midlatitude squall line. *Journal of Atmospheric Scences.*, **52 (11)**, 1934–1948, https://doi.org/10.1175/1520-0469(1995)052 1934:TEOMPO 2.0.CO;2.

Thompson, E. J., Rutledge, S. A., Dolan, B., Thurai, M., & Chandrasekar, V. (2018). Dual-polarization radar rainfall estimation over tropical oceans. *Journal of Applied Meteorology and Climatology*, **57 (3)**, 755–775. https://doi.org/10.1175/JAMC-D-17-0160.1.

Varble, A., & Coauthors. (2011). Evaluation of cloud-resolving model intercomparison simulations using two-ice observations: Precipitation and cloud structure. *Journal of Geophysical Research*, **116 (D12206)**. https://doi.org/10.1029/2010JD015180.

Varble, A., & Coauthors. (2014). Evaluation of cloud-resolving and limited area model intercomparison simulations using two-ice observations: 1. deep convective updraft properties. *Journal of Geophysical Research, [Atmospheres]*, **119 (24)**, 13,891–13,918. https://doi.org/10.1002/2013JD021371.

Wu, D., Dong, X., Xi, B., Feng, Z., Kennedy, A., Mullendore, G., Gilmore, M., & Tao, W.-K. (2013). Impacts of microphysical scheme on convective and stratiform characteristics in two high precipitation squall line events. *Journal of Geophysical Research, [Atmospheres]*, **118**, 11,119–11,135. https://doi.org/10.1002/jgrd.50798.

Yang, M.-J., & Houze, R. A. Jr. (1995). Sensitivity of squall-line rear inflow to ice microphysics and environmental humidity. *Monthly Weather Review*, **123 (11)**, 3175–3193. https://doi.org/10.1175/1520-0493(1995)123 3175:SOSLRI 2 .0.CO;2.

Yuter, S. E., & Houze, R. A. Jr. (1995a). Three-dimensional kinematic and microphysical evolution of Florida cumulonimbus. Part II: Frequency distributions of vertical velocity, reflectivity, and differential reflectivity. *Monthly Weather Review*, **123 (7)**, 1941–1963. https://doi.org/10.1175/1520-0493(1995)123 194 1:TDKAME 2.0.CO;2.

Yuter, S. E., & Houze, R. A. Jr. (1995b). Three-dimensional kinematic and microphysical evolution of Florida cumulonimbus. Part III: Vertical mass transport, mass divergence, and synthesis. *Monthly Weather Review*, **123 (7)**, 1964–1983. https://doi.org/10.1175/1520-0493(1995)123 1964:TDKAME 2.0.CO;2.

Zeng, Z., Yuter, S. E., Houze, R. A. Jr., & Kingsmill, D. E. (2001). Microphysics of the rapid development of heavy convective precipitation. *Monthly Weather Review*, **129 (8)**, 1882–1904, https://doi.org/10.1175/1520-0493(2001)129 1882: MOTRDO 2.0.CO;2.

LIST OF TABLES

Table 1. List of the (left column) 10 observed nocturnal MCSs during the PECAN field campaign analyzed in this study, (middle column) the analysis period for each MCSs, and (right column) the number of size sorting objects identified during the analysis period.

Table 2. List of WRF grid specification, physical parameterizations, and boundary conditions used to simulate the 20 June 2015 PECAN MCS.

Table 3. The change rate in reflectivity values with altitude (dZ/dz, dBZ km^{-1}) from 2 km to 4 km, 4 km to 8 km, and 8 km to 14 km. Shown in the table are the observed dZ/dz (second column from the right) and the WRF-simulated dZ/dz (rightmost column) during the MCS mature and weakening phases.

Table 1. List of the (left column) 10 observed nocturnal MCSs during the PECAN field campaign analyzed in this study, (middle column) the analysis period for each MCSs, and (right column) the number of size sorting objects identified during the analysis period.

Case	Analysis Period (UTC)	Number of Size Sorting Objects Identified
5 June 2015	5:00–11:00	270
11 June 2015	1:30–9:30	581
12 June 2015	4:00–10:00	535
17 June 2015	2:00–9:00	147
20 June 2015	3:00–9:30	321
26 June 2015	2:30–10:30	528
6 July 2015	1:30–7:00	372
9 July 2015	2:00–9:00	695
14 July 2015	3:00–8:00	242
15 July 2015	0:00–9:00	305

Table 2. List of WRF grid specification, physical parameterizations, initial and boundary conditions used to simulate the 20 June 2015 MCS.

Item	Outer domains	Innermost domain	Reference
Grid spacing	27 km, 9 km	3 km	
Domain dimensions	4185 km x 4185 km, 2430 km x 2430 km	1335 km x 1002 km	
Vertical sigma levels	55, 55	55	
Model top pressure	100 hPa, 100 hPa	100 hPa	
ICs and LBCs	NARR	NARR	
Microphysics	NSSL two-moment	NSSL two-moment	Mansell et al.
Cumulus parameterization	Kain-Fritsch	None	Kane (2004)
Longwave radiation	RRTM	RRTM	Mlawer et al. (
Shortwave radiation	Dudhia	Dudhia	Dudhia (1989)
Surface layer	Eta similarity	Eta similarity	Janjic (1994)
Land surface model	Unified Noah	Unified Noah	Tewari et al. (
Boundary layer physics	MYJ	MYJ	Janjic (1994)

Table 3. The change of radar reflectivity with altitude (dZ/dz; dBZ km^{-1}) in three vertical layers (2–4 km, 4–8 km, and 8–14 km, repsectively). Shown are the observed dZ/dz and the WRF-simulated dZ/dz during the MCS mature and weakening phases.

		dZ/dz (dBZ km^{-1})	
	Layer	Observed	WRF
Mature	2–4 km	–1.55	–1.82
	4–8 km	–2.80	–2.46
	8–14 km	–2.61	–5.71
Weakening	2–4 km	–1.66	–2.21
	4–8 km	–3.80	–3.51
	8–14 km	–1.80	–4.43

LIST OF FIGURES

Figure 1: Domain setting used to simulate the 20 June 2015 PECAN MCS.

Figure 2: Example of size-sorting object identification. Colored are radar observations of (a) Z_{DR} and (b) K_{DP} at 1-km height. Red contours are the areas where Z_{DR} values exceed the 95th percentile, and white contours are the areas where K_{DP} values exceed the 93th percentile. For contour objects that also exceed a 75th size percentile, the contour centroids are marked with square markers.

Figure 3: PECAN MCSs composite bivariate scatter distributions of the separation distance of each size sorting objects and (a) the collocated 75th percentile of 20-dBZ echo top height (in km) and (b) liquid water mass (in g m^{-3}) at 3.5-km height. Superposed to the scatter plots are the normalized frequency distributions, plotted with an interval of 0.1.

Figure 4: Same as Figure 3, but for (a) precipitation rates at 25th percentile, (b) precipitation rates at 50th percentile, (c) precipitation rates at 75th percentile, and (d) precipitation rates at 95th percentile.

Figure 5: Model validation of the 20 June PECAN MCS. The upper row shows the NEXRAD reflectivity mosaic of the column-maximum reflectivity maps, valid at (a) 0600 UTC, (b) 0700 UTC, (c) 0800 UTC, (d) 0900 UTC, and (e) 1100 UTC. The lower row is the WRF-simulated column-maximum reflectivity maps (lowf, g, h, i, j), valid at the identical times as those shown in upper row.

Figure 6: Hovmoller (longitude-time) diagram of the (a) Stage IV hourly precipitation (in mm) and (b) the WRF-simulated hourly precipitation (in mm) within the analysis domain of 105.5°W–95°W, 42.5°N–46.5°N.

Figure 7: Panel in the upper row show the (a) observed reflectivity CFAD and (b) WRF-simulated reflectivity CFAD during the MCS mature phase (0600–1000 UTC). Panels in the lower row show the (c) observed reflectivity CFAD and (d) WRF-simulated reflectivity CFAD during the MCS weakening phase (1000–1200 UTC).

Figure 8: Upper row shows the KABR-KFSD composite of (a) column-maximum reflectivity, (b) 4-km vertical velocity retrieved from KABR-KFSD radial velocities, (c) 1-km Z_{DR} (color; dB) and K_{DP} (yellow contours; plotted at 1.75, 1.9, and 2.05 deg km^{-1}). Vectors in panels (a)-(c) are the mean low-level (1–4 km) system-relative winds. Gray shadings in panels (a-c) are the KABR-KFSD dual-Doppler lobes where dual-Doppler winds cannot be retrieved. Panels in the lower panel (d-e) are similar to panels (a-b), but for the WRF simulation. Panel (f) shows the rain concentration at logarithmic scale (colored) and rain diameter (mm; contoured), both valid at the lowest model level (~20 m).

Figure 9: (a) Bivariate scatters of separation distances versus echo top heights and normalized frequency distribution for the observed 20 June 2015 PECAN

MCS. (b) Simulated bivariate scatters and normalized frequency distribution of separation distances and echo top heights. (c) Simulated bivariate scatters and normalized frequency distribution of ice water path (IWP; blue scatters and contours) and liquid water path (LWP; orange scatters and contours). Three object categories defined in the text are color-highlighted in (b).

Figure 10: Probability density functions (PDFs) of the precipitation rates near size-sorting objects with d_{WRF}>10.5 km (red solid line) and those near size-sorting objects with d_{WRF} between 7.5 km and 10.5 km (blue dashed line) during the MCS mature phase (0600–1000 UTC).

Figure 11: Simulated bivariate distributions of separation distances and integrated microphysical heating/cooling terms. Panels in the upper row show the object-collocated values (scatters) and the normalized frequency distributions of (a) integrated deposition heating, (b) integrated freezing heating, and (c) integrated condensation heating. Panels in lower row show the object-collocated values (scatters) and the normalized frequency distributions of (d) integrated sublimation cooling, (e) integrated melting cooling, and (f) integrated evaporation cooling.

Figure 12: The differences between the CFADs for objects with d_{WRF}>10.5 km (objects within rectangle III in Figure 9b) and objects with 7.5 km < d_{WRF} <10.5 km (objects within rectangle II in Figure 9b) and the two-sample K-S test p-values at different temperature levels. The variable analyzed in panel (a) is the freezing heating (in logarithmic scale), and the variable analyzed in panel (b) is the melting cooling (in logarithmic scale). Black dashed vertical lines in the K-S p-value panels represent the K-S significant threshold, i.e. p-value less than 0.05. Gray dashed line in each panel represents the 0°C level.

Figure 13: Similar to Figure 12, but for (a) deposition heating, (b) condensation heating, (c) absolute sublimation cooling, and (d) absolute evaporative cooling. All heating and cooling terms are in logarithmic scale.

Figure 14: Similar to Figure 12, but for (a) updraft intensity and (b) absolute downdraft intensity.

Figure 15: Simulated mean spatial distributions of different variables at different heights within the 12-km diameter circles surrounding the midpoint between D_{mr} and N_{Tr} centroids, shown in polar coordinates. The variables analyzed in each panel is (a) graupel diameter (in mm) at 4-km height, (b) graupel number concentration (in m^{-3}) at 4-km height, (c) vertical velocity (in m s^{-1}) at 4-km height, (d) rain diameter (in mm) at 0.25-km height, and (e) rain number concentration (in m^{-3}) at 0.25-km height.

Figure 16: (a) Vertical profile of 95th percentile rain mass (in g kg^{-1}) generated from the cold pathway (solid lines) and the warm pathway (dashed lines) for objects with d_{WRF}>10.5 km (black-colored lines) and objects with 7.5 km < d_{WRF} <10.5 km (red-colored lines). Celsius temperature is used in the vertical axis. (b) Similar to the panels in the upper row of Figure 15, but for the relative

humidity (in %) at 4-km height.

Figure 17: Schematic diagram of the microphysical processes leading to (a-c) larger low-level separation distances and (d-f) smaller low-level separation distances proposed in Section 6.

Figure A1: Mean spatial distributions of (a) graupel diameter (in mm) at 4-km height and (b) graupel number concentration (in m^{-3}) at 4-km height surrounding size-sorting objects for the simulation with an extra inner domain with 1-km grid spacing (CTRL-1 km). Bivariate scatter plots and normalized frequency distributions between separation distances and (c) echo top height and (d) integrated freezing heating from the CTRL-1 km simulation.

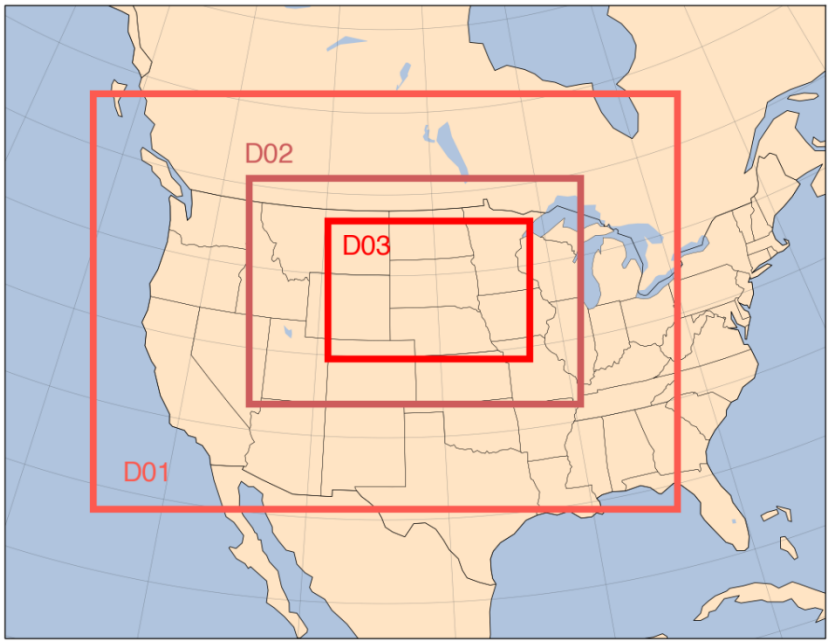

Figure 1: Domain setting used to simulate the 20 June 2015 PECAN MCS.

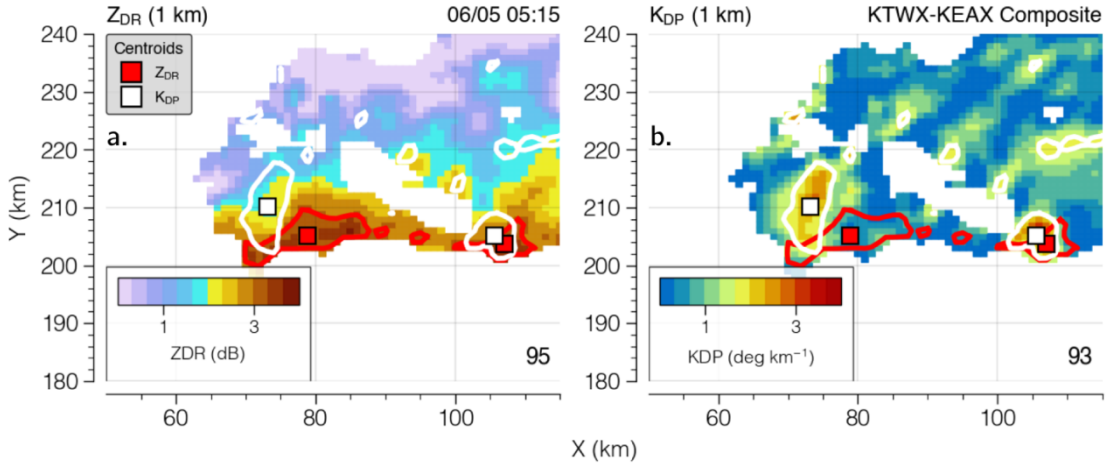

Figure 2: Example of size-sorting object identification. Colored are radar observations of (a) Z_{DR} and (b) K_{DP} at 1-km height. Red contours are the areas where Z_{DR} values exceed the 95th percentile, and white contours are the areas where K_{DP} values exceed the 93th percentile. For contour objects that also exceed a 75th size percentile, the contour centroids are marked with square markers.

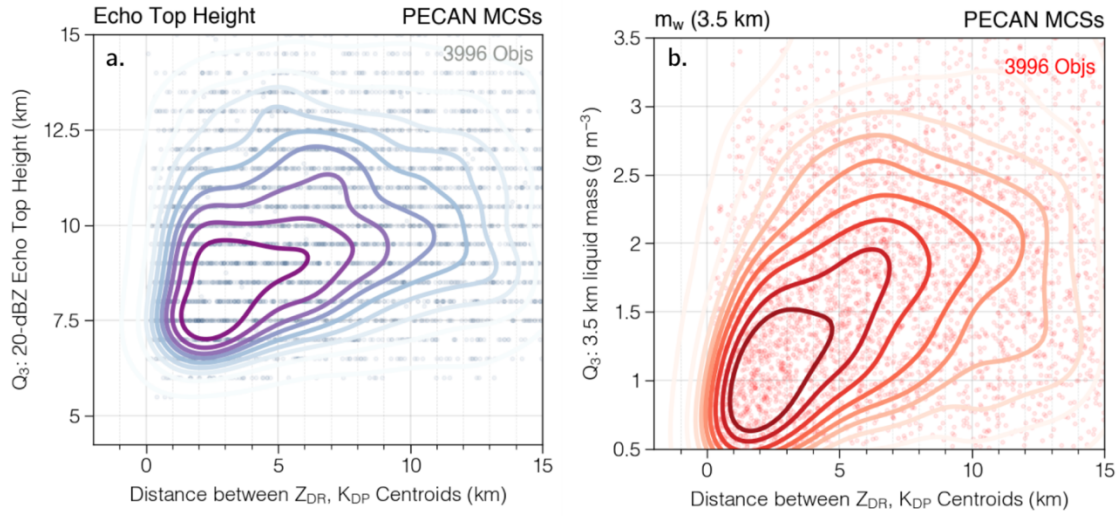

Figure 3: PECAN MCSs composite bivariate scatter distributions of the separation distance of each size sorting objects and (a) the collocated 75th percentile of 20-dBZ echo top height (in km) and (b) liquid water mass (in g m^{-3}) at 3.5-km height. Superposed to the scatter plots are the normalized frequency distributions, plotted with an interval of 0.1.

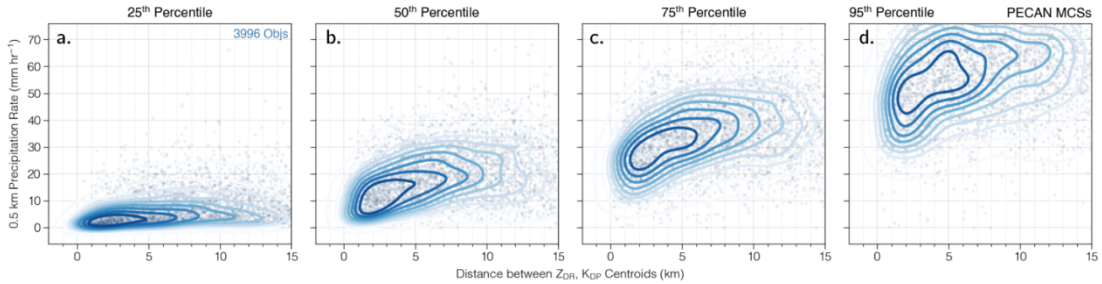

Figure 4: Same as Figure 3, but for (a) precipitation rates at 25th percentile, (b) precipitation rates at 50th percentile, (c) precipitation rates at 75th percentile, and (d) precipitation rates at 95th percentile.

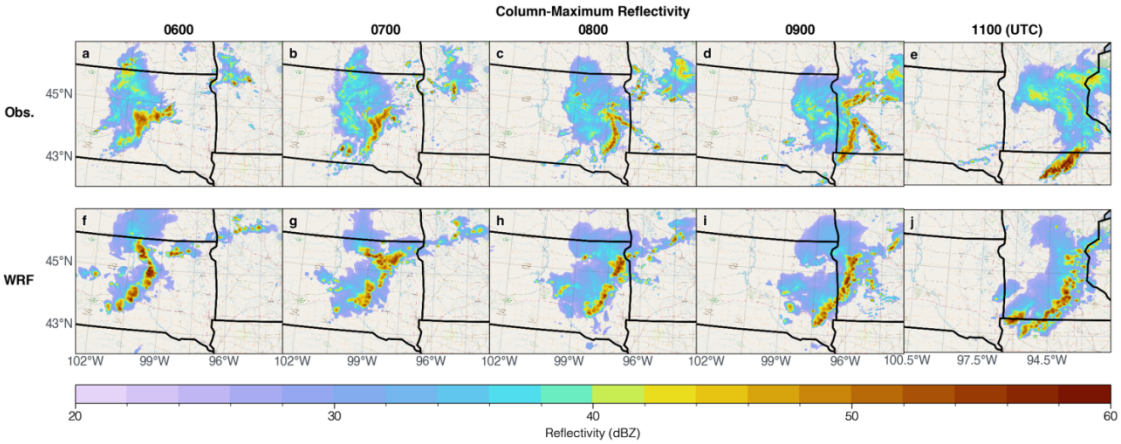

Figure 5: Model validation of the 20 June PECAN MCS. The upper row shows the NEXRAD reflectivity mosaic of the column-maximum reflectivity maps, valid at (a) 0600 UTC, (b) 0700 UTC, (c) 0800 UTC, (d) 0900 UTC, and (e) 1100 UTC. The lower row is the WRF-simulated column-maximum reflectivity maps (lowf, g, h, i, j), valid at the identical times as those shown in upper row.

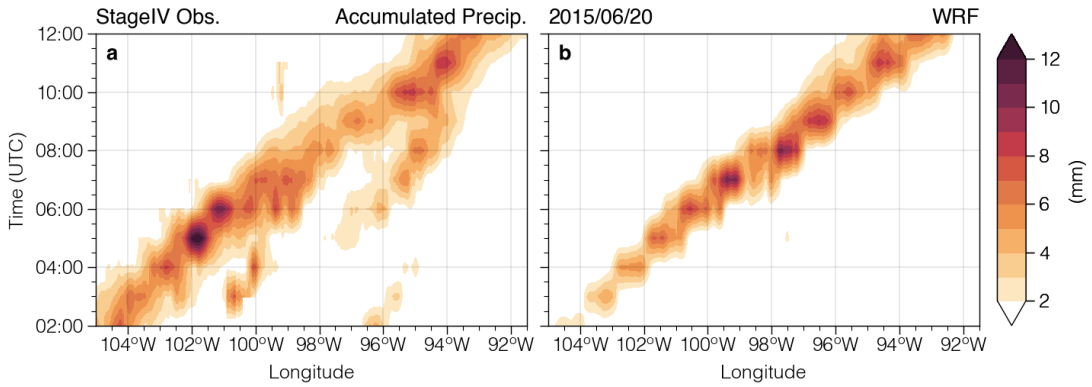

Figure 6: Hovmoller (longitude-time) diagram of the (a) Stage IV hourly precipitation (in mm) and (b) the WRF-simulated hourly precipitation (in mm) within the analysis domain of 105.5°W–95°W, 42.5°N–46.5°N.

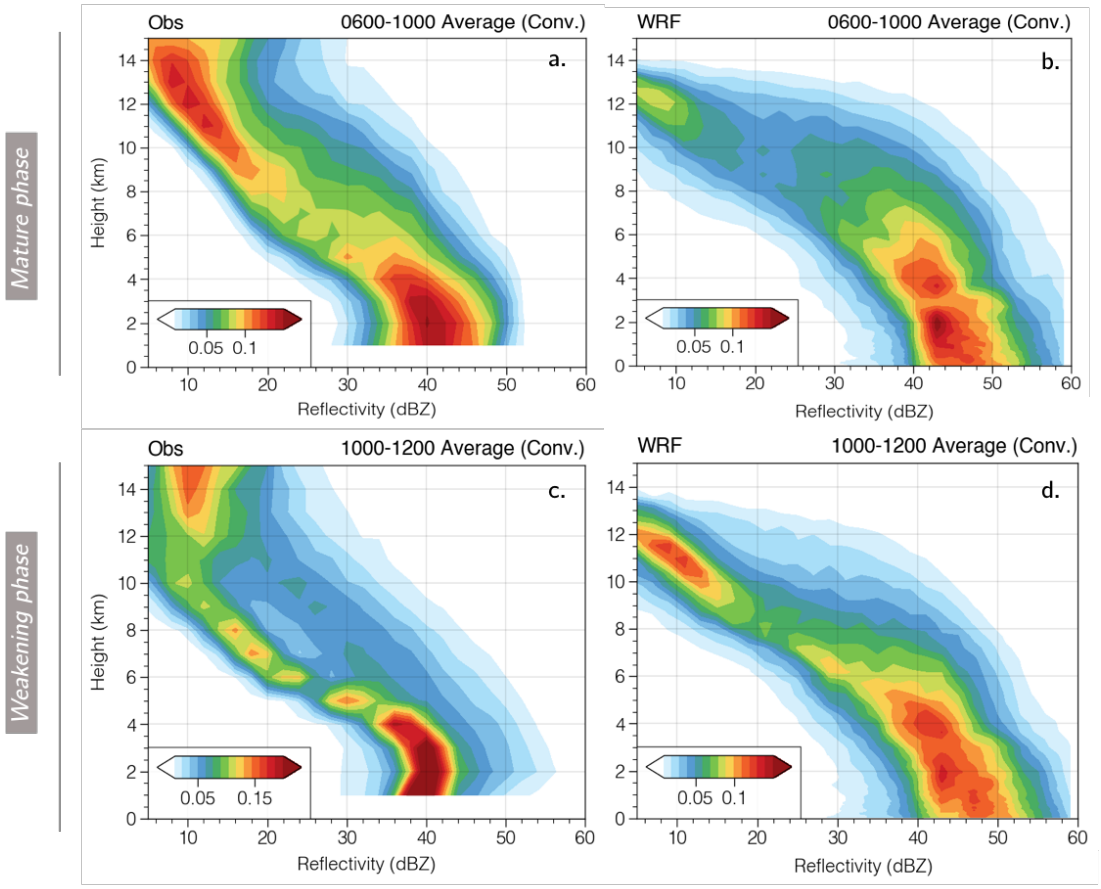

Figure 7: Panels in the upper row show the (a) observed reflectivity CFAD and (b) WRF-simulated reflectivity CFAD during the MCS mature phase (0600–1000 UTC). Panels in the lower row show the (c) observed reflectivity CFAD and (d) WRF-simulated reflectivity CFAD during the MCS weakening phase (1000–1200 UTC).

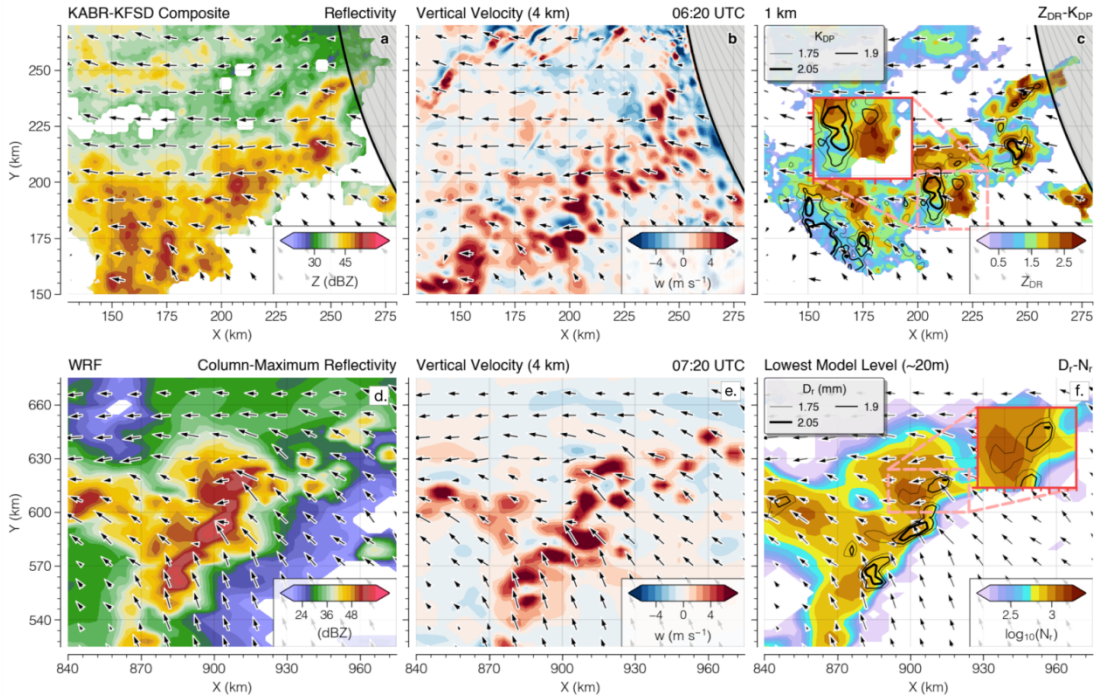

Figure 8: Upper row shows the KABR-KFSD composite of (a) column-maximum reflectivity, (b) 4-km vertical velocity retrieved from KABR-KFSD radial velocities, (c) 1-km Z_{DR} (color; dB) and K_{DP} (yellow contours; plotted at 1.75, 1.9, and 2.05 deg km^{-1}). Vectors in panels (a)-(c) are the mean low-level (1–4 km) system-relative winds. Gray shadings in panels (a-c) are the KABR-KFSD dual-Doppler lobes where dual-Doppler winds cannot be retrieved. Panels in the lower panel (d-e) are similar to panels (a-b), but for the WRF simulation. Panel (f) shows the rain concentration at logarithmic scale (colored) and rain diameter (mm; contoured), both valid at the lowest model level (~20 m).

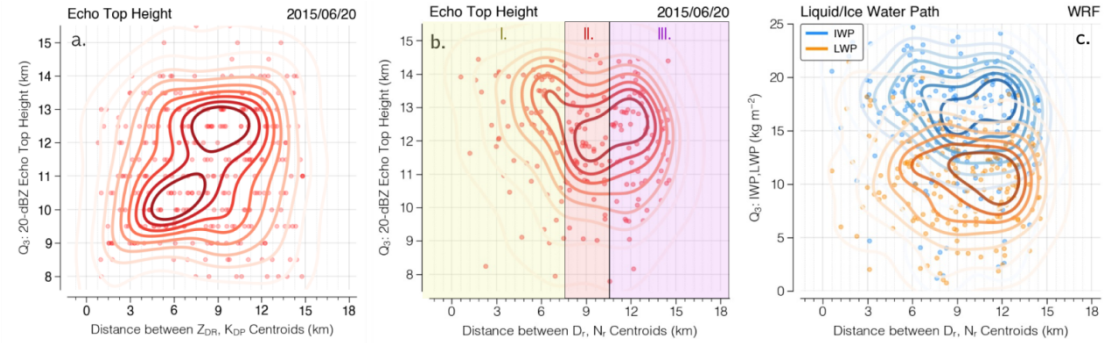

Figure 9: (a) Bivariate scatters of separation distances versus echo top heights and normalized frequency distribution for the observed 20 June 2015 PECAN MCS. (b) Simulated bivariate scatters and normalized frequency distribution of separation distances and echo top heights. (c) Simulated bivariate scatters and normalized frequency distribution of ice water path (IWP; blue scatters and contours) and liquid water path (LWP; orange scatters and contours). Three object categories defined in the text are color-highlighted in (b).

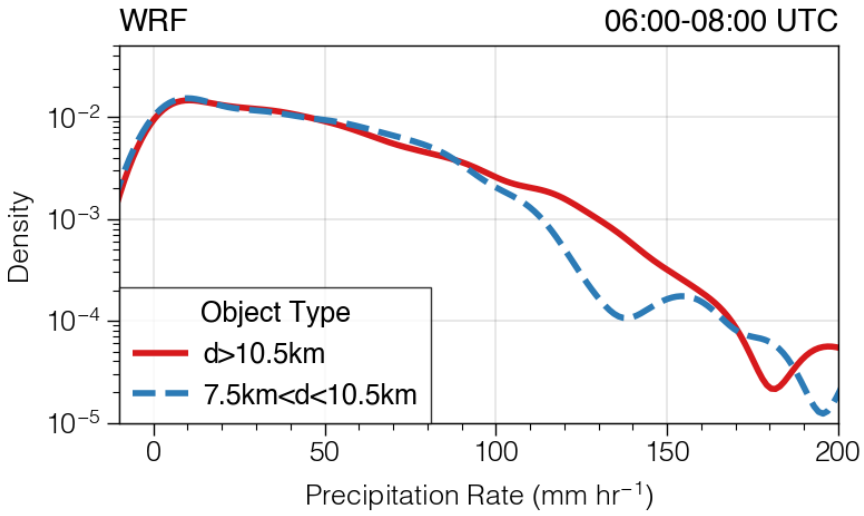

Figure 10: Probability density functions (PDFs) of the precipitation rates near size-sorting objects with d_{WRF}>10.5 km (red solid line) and those near size-sorting objects with d_{WRF} between 7.5 km and 10.5 km (blue dashed line) during the MCS mature phase (0600–1000 UTC).

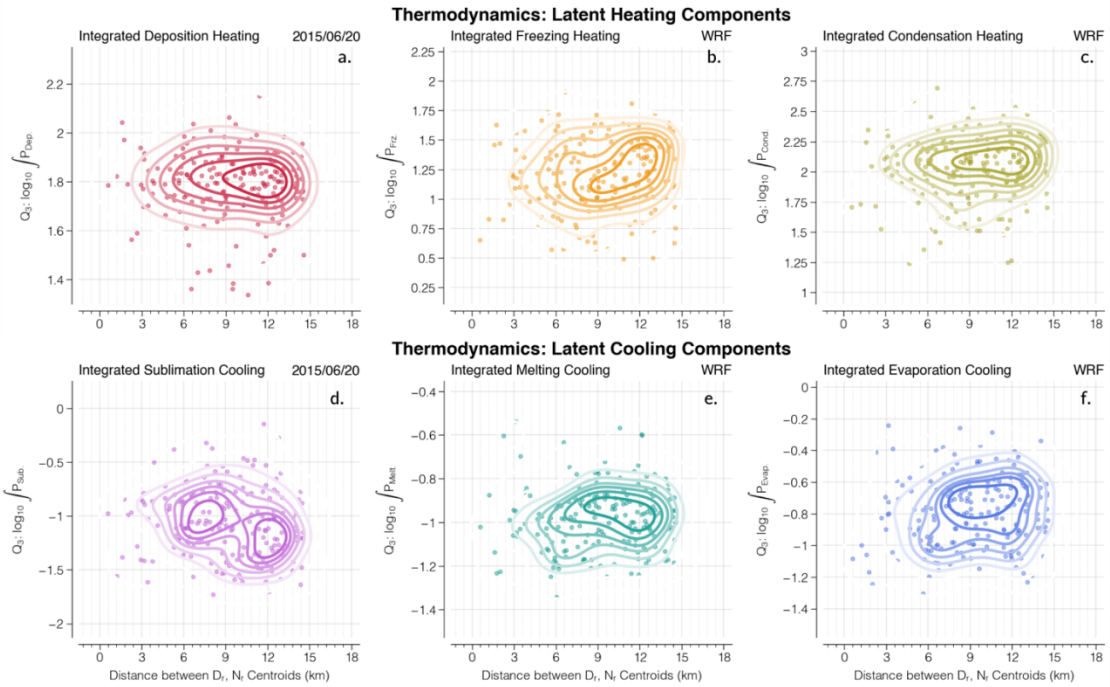

Figure 11: Simulated bivariate distributions of separation distances and integrated microphysical heating/cooling terms. Panels in upper row show the object-collocated values (scatters) and the normalized frequency distributions of (a) integrated deposition heating, (b) integrated freezing heating, and (c) integrated condensation heating. Panels in lower row show the object-collocated values (scatters) and the normalized frequency distributions of (d) integrated sublimation cooling, (e) integrated melting cooling, and (f) integrated evaporation cooling.

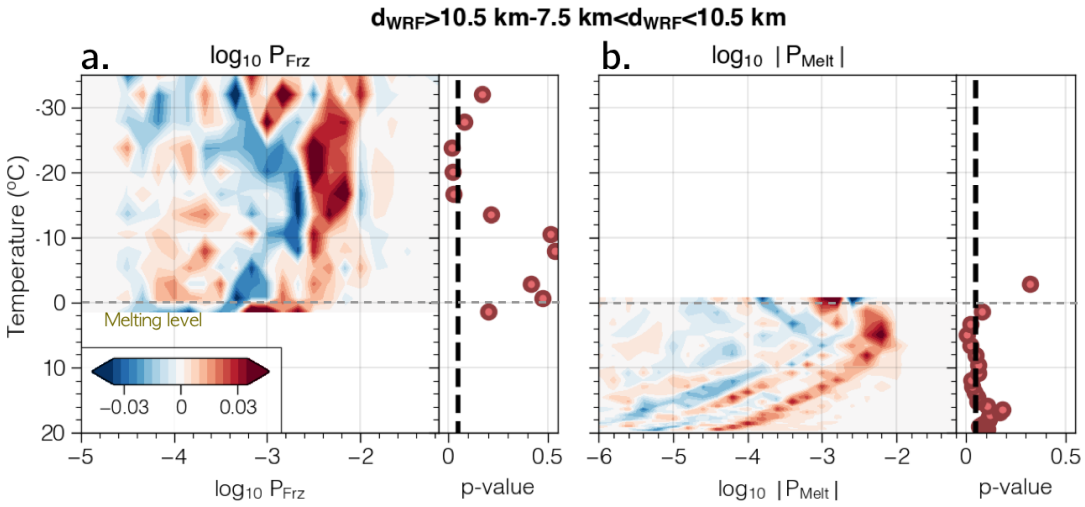

Figure 12: The differences between the CFADs for objects with d_{WRF}>10.5 km (objects within rectangle III in Figure 9b) and objects with 7.5 km < d_{WRF} <10.5 km (objects within rectangle II in Figure 9b) and the two-sample K-S test p-values at different temperature levels. The variable analyzed in panel (a) is the freezing heating (in logarithmic scale), and the variable analyzed in panel (b) is the melting cooling (in logarithmic scale). Black dashed vertical lines in the K-S p-value panels represent the K-S significant threshold, i.e. p-value less than 0.05. Gray dashed line in each panel represents the 0°C level.

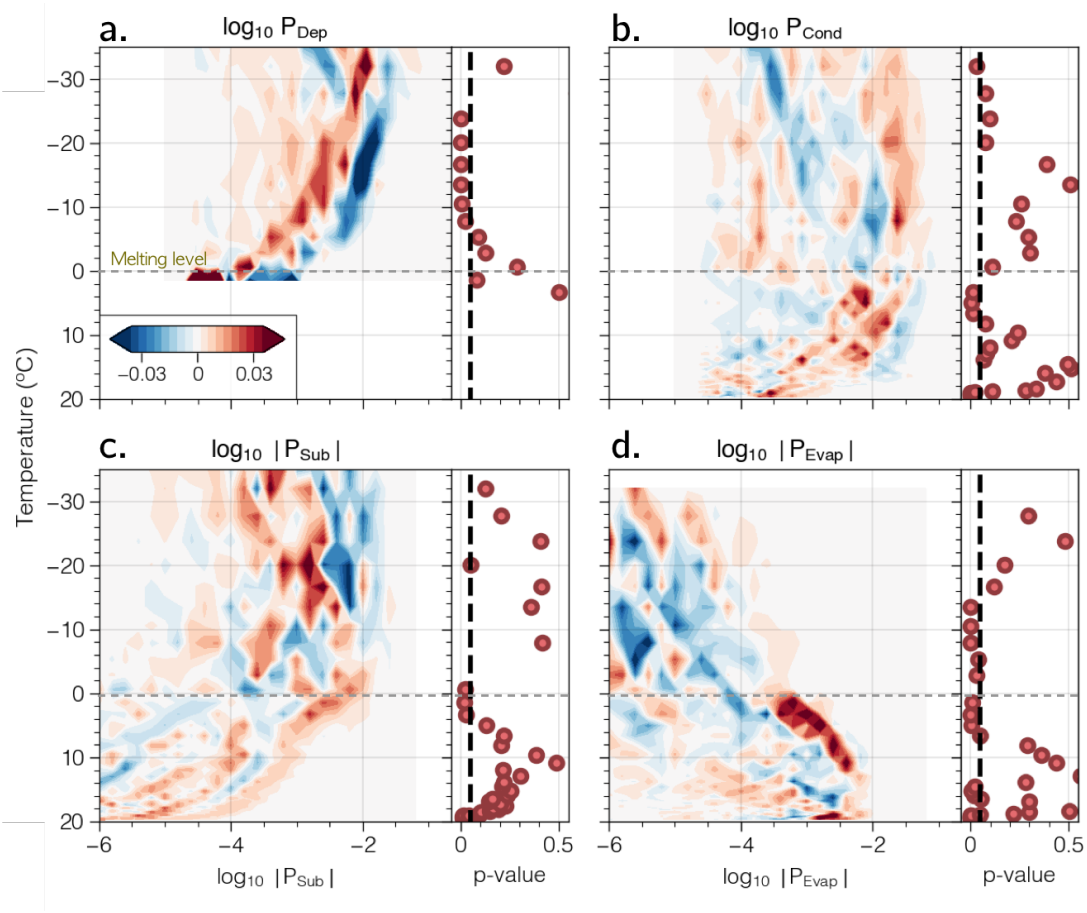

Figure 13: Similar to Figure 12, but for (a) deposition heating, (b) condensation heating, (c) absolute sublimation cooling, and (d) absolute evaporative cooling. All heating and cooling terms are in logarithmic scale.

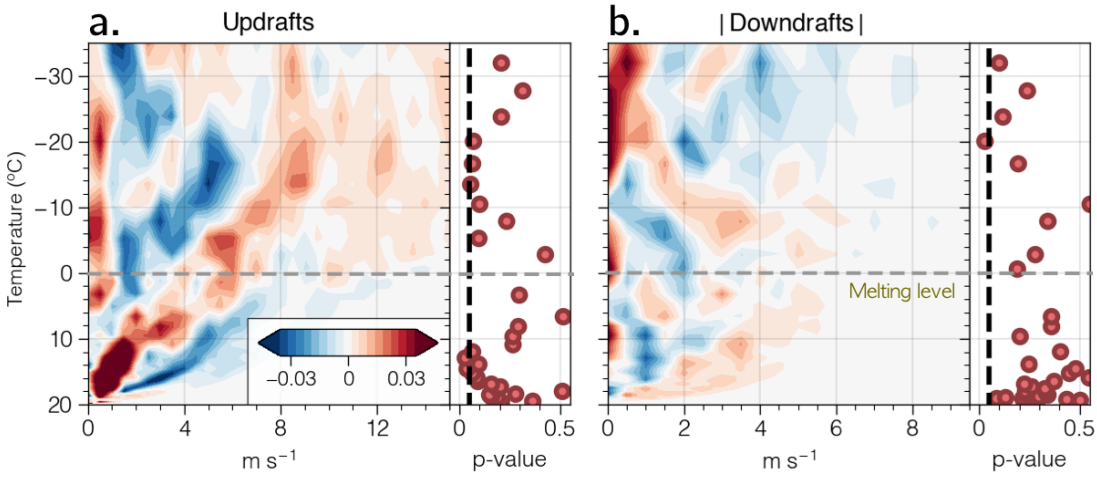

Figure 14: Similar to Figure 12, but for (a) updraft intensity and (b) absolute downdraft intensity.

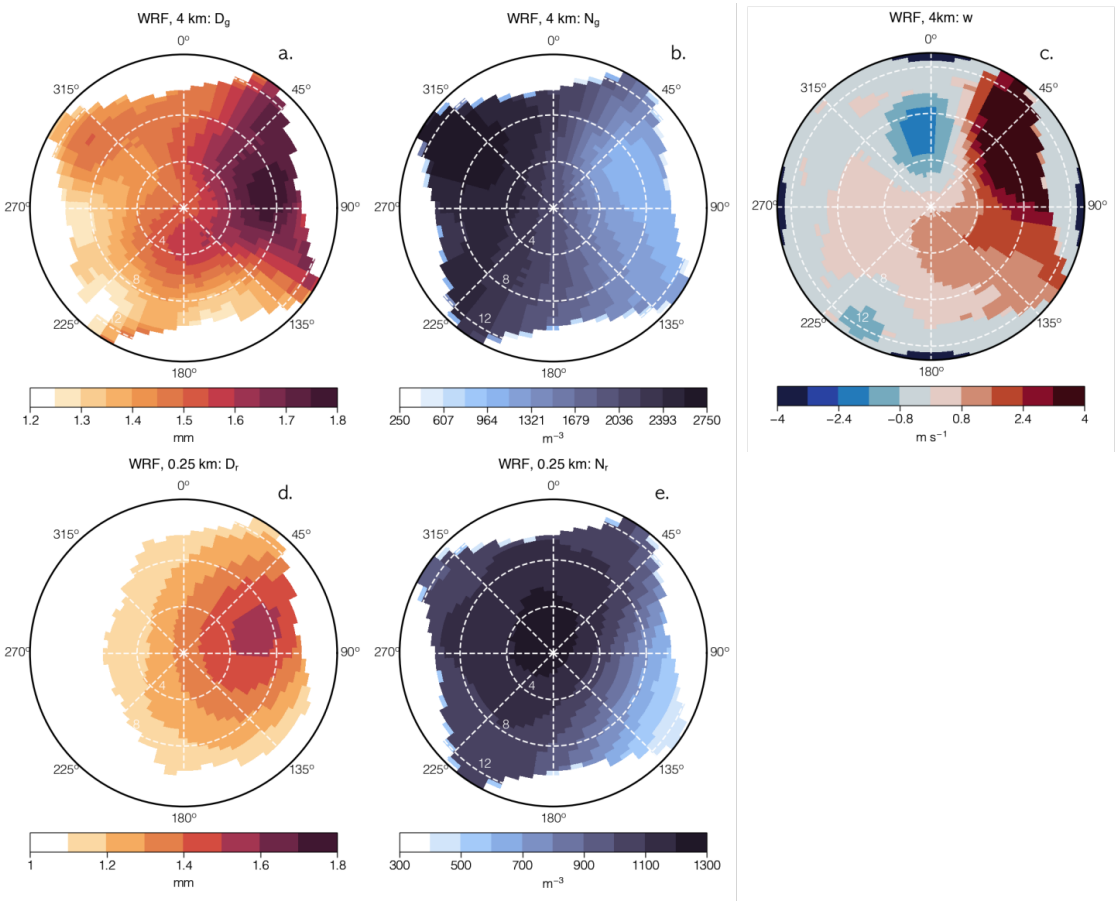

Figure 15: Simulated mean spatial distributions of various variables at different heights within the 12-km diameter circles surrounding the midpoint between D_{mr} and N_{Tr} centroids, shown in polar coordinates. The variables analyzed in each panel is (a) graupel diameter (in mm) at 4-km height, (b) graupel number concentration (in m^{-3}) at 4-km height, (c) vertical velocity (in m s^{-1}) at 4-km height, (d) rain diameter (in mm) at 0.25-km height, and (e) rain number concentration (in m^{-3}) at 0.25-km height.

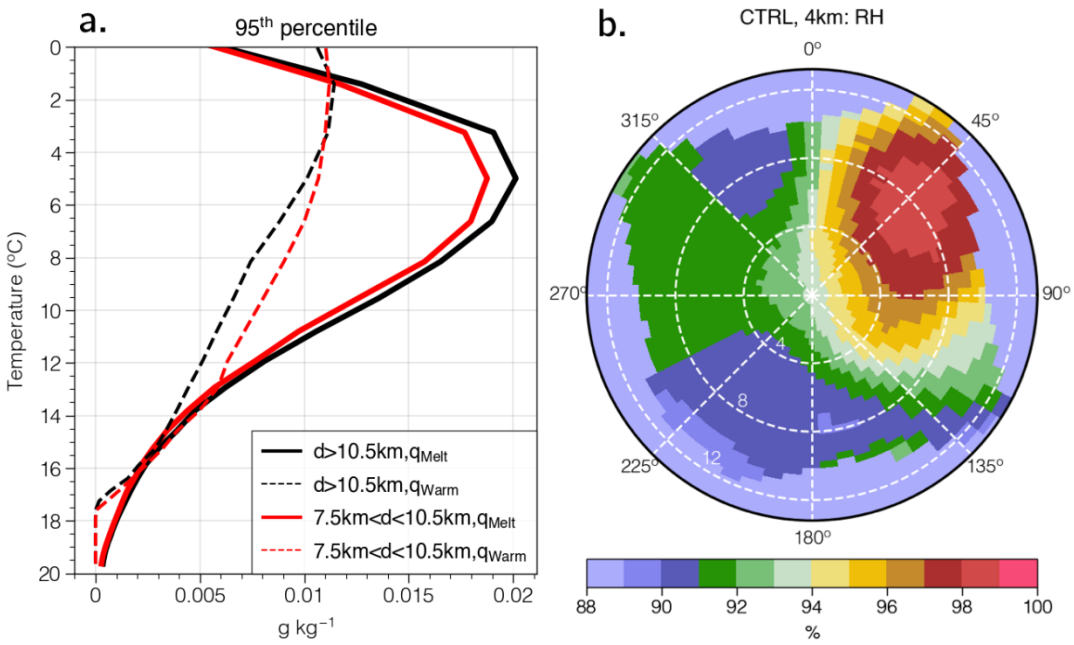

Figure 16: (a) Vertical profile of 95th percentile rain mass (in g kg^{-1}) generated from the cold pathway (solid lines) and the warm pathway (dashed lines) for objects with d_{WRF}>10.5 km (black-colored lines) and objects with 7.5 km < d_{WRF} <10.5 km (red-colored lines). Celsius temperature is used in the vertical axis. (b) Similar to the panels in the upper row of Figure 15, but for the relative humidity (in %) at 4-km height.

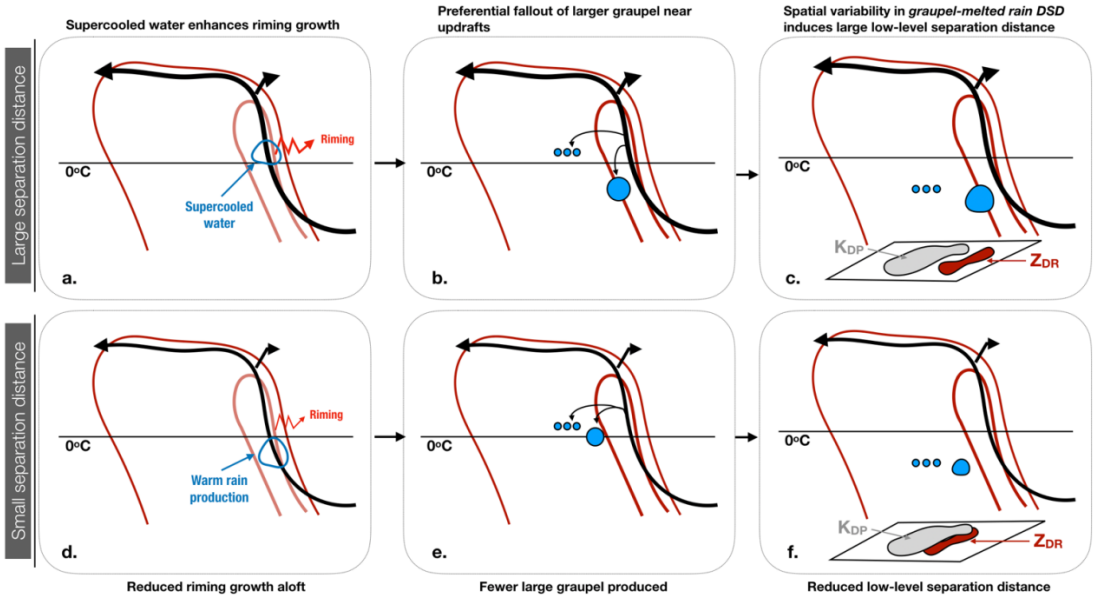

Figure 17: Schematic diagram of the microphysical processes leading to (a-c) larger low-level separation distances and (d-f) smaller low-level separation distances proposed in Section 6.

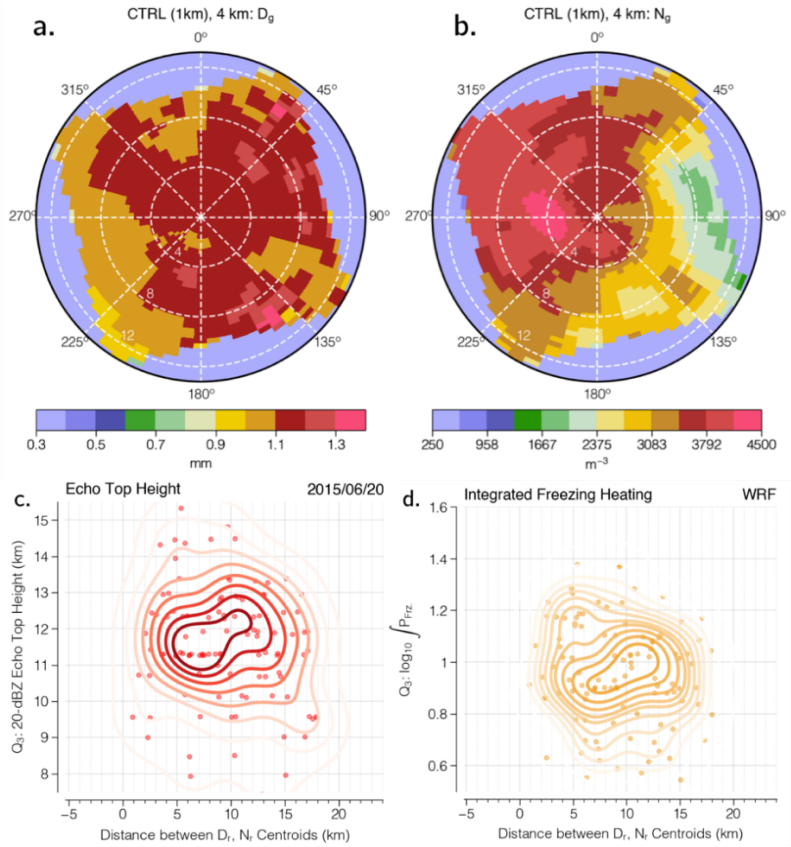

Figure A1: Mean spatial distributions of (a) graupel diameter (in mm) at 4-km height and (b) graupel number concentration (in m^{-3}) at 4-km height surrounding size-sorting objects for the simulation with an extra inner domain with 1-km grid spacing (CTRL-1 km). Bivariate scatter plots and normalized frequency distributions between separation distances and (c) echo top height and (d) integrated freezing heating from the CTRL-1 km simulation.